Adaptive Superresolution in Deconvolution of Sparse Peaks

Alexandra Koulouri, Pia Heins and Martin Burger

Abstract

The aim of this paper is to investigate superresolution in deconvolution driven by sparsity priors. The observed signal is a convolution of an original signal with a continuous kernel. With the prior knowledge that the original signal can be considered as a sparse combination of Dirac delta peaks, we seek to estimate the positions and amplitudes of these peaks by solving a finite dimensional convex problem on a computational grid. Because, the support of the original signal may or may not be on this grid, by studying the discrete deconvolution of sparse peaks using ℓ_1-norm sparsity prior, we confirm recent observations that canonically the discrete reconstructions will result in multiple peaks at grid points adjacent to the location of the true peak. Owning to the complexity of this problem, we analyse carefully the de-convolution of single peaks on a grid and gain a strong insight about the dependence of the reconstructed magnitudes on the exact peak location. This in turn allows us to infer further information on recovering the location of the exact peaks i.e. to perform super-resolution. We analyze in detail the possible cases that can appear and based on our theoretical findings, we propose an self-driven adaptive grid approach that allows to perform superresolution in one-dimensional and multi-dimensional spaces. With the view that the current study can provide a further step in the development of more robust algorithms for the detection of single molecules in fluorescence microscopy or identification of characteristic frequencies in spectral analysis, we demonstrate how the proposed approach can recover sparse signals using simulated clusters of point sources (peaks) of low-resolution in one and two dimensional spaces.

Index Terms

Deconvolution, superresolution, sparsity, ℓ_1-norm prior, LASSO problem, first order optimality condition, grid, discetization, node, element, smooth and symmetric kernel.

A. Koulouri was with the Faculty of Information Technology and Communication Sciences, Tampere University, P.O. Box 692, 33101 Tampere, FI, e-mail: alexandra.koulouri@tuni.fi.

Pia Heins was with Faculty of Electrical Engineering and Information Technology, University of Applied Sciences and Arts Hannover, Ricklinger Stadtweg 120, 30459 Hannover, DE e-mail: pia.heins@hs-hannover.de

Martin Burger was with the Department of Mathematics, Universität Erlangen-Nürnberg, Cauerstrasse 11, 91058 Erlangen, DE, e-mail: martin.burger@fau.de

I. INTRODUCTION

A. *Deconvolution of sparse peaks on discrete grids*

In a wide range of imaging applications, the signal of interest comprises a sequence of sparse peaks (or point sources) for instance in fluoresce microscopy [45], [55], [72], astronomy [52], ultrasound or Doppler technology [78], [79], [4], [6], medical imaging [76], [14] and computational neuroscience [33]. In these applications, one has frequently to solve the problem that the signal of interest cannot be observed directly, but has to be inferred from other quantities, often low spatial resolution observations which mathematically can be described as the convolution of the original signal with a smooth kernel.

In this article, we study the superresolution problem, known as sparse peak deconvolution [29], where one seeks to estimate the positions and amplitudes of the underlying sparse peaks from a set of blurred observations. As idealized data we consider the convolution of a measure μ on $\Omega \subseteq \mathbb{R}^d$ with a known symmetric and smooth (with infinite support) kernel G which attains its maximum at 0, i.e.

$$f(x) = (G * \mu)(x) := \int_\Omega G(x-y) \, d\mu(y) \, . \tag{I.1}$$

Here we consider the convolution operator from $\mathcal{M}(\Omega)$ to $L^2(\Omega)$, which is well-defined by the Fourier convolution theorem (cf. [19]) and we are interested in the reconstruction of sparse peaks when the corresponding original signal is of the form

$$\mu(x) = \sum_{l=1}^{L} \gamma_l \delta_{\xi_l} \, , \tag{I.2}$$

where L is the total number of peaks and $\delta_{\xi_l} = \delta(x-\xi_l)$ denotes a concentrated measure (expressed through the Dirac-delta function δ) at location $\xi_l : \Omega \to \mathbb{R}^d$ with amplitude γ_l.

In order to obtain a sparse reconstruction it is nowadays standard to employ the well-established ℓ_1-norm minimization approaches (also known as Basic Pursuit or LASSO) [24], [67], [20] which, in addition to sparse promoting solutions, allow the linearization of the original problem, the direct application of fast convex optimization solvers (e.g. [38]) and do not require application of Fourier transform[16]. So, instead of solving a continuous deconvolution problem [21], [15], [13], [16], the aim is to reconstruct μ via a discrete set of concentrated measures, i.e to look for a discrete

solution of the form

$$\mu^N(x) = \sum_{k=1}^{N} c_k \delta_{x_k} , \qquad (I.3)$$

where $c = \{c_k\}_{k=1,...,N} \in \mathbb{R}^N$ is a vector that contains the numerically estimated amplitudes (weights) at a set of grid points $\{x_k\}_{k=1,...,N}$. With the discretization of the computational domain, the convolution can be written as an operator acting on the coefficients $c = \{c_k\}_{k=1,...,N}$, i.e.

$$G * \mu^N = Ac = \sum_{k=1}^{N} c_k G(x - x_k) , \qquad (I.4)$$

where $A : \mathbb{R}^N \to L^2(\Omega)$. The ℓ_1-norm minimization problem is

$$\min_{c \in \mathbb{R}^N} \ J(c) := \frac{1}{2}\|Ac - f\|^2 + \lambda\|c\|_1 . \qquad (I.5)$$

Since the support of signal μ (I.2) may or may not be on the computational grid $\{x_k\}_{k=1,...,N}$, three chief questions for the ℓ_1-norm estimates arise:

- How the error between the original signal μ and discrete signal μ^N is quantified based on the discretization?
- What are the expected patterns of the discrete estimation μ^N on an arbitrary grid?
- Can the locations and amplitudes of the original signal μ be approximated with the help of the solution μ^N?

In this article, we investigate and answer these questions with the help of convex optimization theory and standard numerical analysis. We anticipate that the understanding of the effects of sparsity promoting solvers when the computational grid and the support of the original sparse signal do not coincide will allow the development of more robust algorithms required in applications such as fluorescence microscopy [34], [70], [69], [40], [37], [72], [43], [61].

B. Related works

Sparsity prior driven deconvolution approaches in continuous domains have been studied in several works including [21], [15], [13], [27], [36]. The signal (sum of Dirac functions) to be recovered is not a finite-dimensional vector (as in (I.3)) but a Radon measure and the minimization problem is formulated with the help of the total variation (TV) term and this problem is referred to as Beurling-Lasso (BLASSO) [21], [27], [65]. An extensive theoretical analysis of BLASSO in the case of one dimensional Fourier measurements was provided in [16]. Particularly, it was shown

that if the spikes are separated enough, then the exact recovery is possible (when the fraction of the measurement noise and regularization parameter tends to zero). Robustness to noise under this separation condition was studied by [3], [27], while the effect of the positivity constraint was analyzed in [8], [56], [22], [31], [30]. The observation sampling and the exact support recovery was theoretically studied in [25]. In [65], the BLASSO problem was analyzed for measures in higher dimensional spaces revealing that the kernel and arrangement of the original peaks affect the stability in the estimates.

BLASSO is a convex but infinite dimensional optimization problem. As shown in [16], [9], [75], [7], [36], solvers exist for ideal lowpass filters (i.e. Dirichlet type of kernels) when the observations are transformed into the Fourier domain and consider a finite number of frequencies in one dimensional signal spaces. Particularly, in theses cases, the primal (BLASSO) problem is expressed via its (Fenchel-Rockafellar) associated finite dimensional dual problem, which for the numerical computations is encoded as a finite semi-definite program (SDP) [16], [18]. The core of these approaches rely on the duality between peak locations and the existence of an interpolating trigonometric polynomial (often referred to as dual certificate) in the measurement (dual) space (which is bounded by 1 in magnitude at locations indicating the underlying peaks [17]). However, apart from the one dimensional spaces (line and torus), there is not a canonical extension or exact SPD formulation in higher dimensional spaces. We refer for instance to [18] (and the references therein) for relaxed SDP versions in higher dimensions.

In arbitrary spaces and for general kernels, one has to approximate the BLASSO problem by first introducing discrete grids and then solve a finite dimensional minimization problem (e.g. LASSO or basic pursuit). Several authors have proposed approximation or non-convex optimization steps to be included in the standard LASSO to recover the exact locations and amplitudes. In particular, in [32], [29], the continuous basis-pursuit which involves a first order Taylor approximation of the kernel in the fidelity term of the minimization problem accompanied by the ℓ_1-norm regularization term have been utilized to improve the accuracy in the peak localization. However, multiple peaks around the original peak is a common result (as also theoretically justified in [29]). More robust iterative approaches using the Frank-Wolfe algorithm (also known as conditional gradient method) has been proposed in [13], [10]. These include an alternation between two steps. In the first step, the computational support is renewed by generating a new peak location using the conditional gradient method and then a non-convex step follows where only the locations and amplitudes are computed

while the number of peak locations stays fixed.

Even though the current paper is focusing on superresolution using convex optimization methods and especially the ℓ_1-norm regularization, we would like to mention that there is also a vast literature on spectral superresolution algorithms that rely on Prony's concept (for a general review see [49], [73]), for example MUSIC [71], ESPRIT [66]) or pencil method [44]. These methods perform well in noiseless setting and do not require a minimum separation condition to fully recover positive and negative peaks; however they rely strongly on the signal, noise and measurement modelling and their extension to higher dimension is not trivial see e.g. [53], [63], [50], [2], [51], [23].

C. Contributions

In this work, the aim is to find new connections between the super-resolution algorithms which impose sparsity assumptions on the signal to be recovered [72] and theoretical studies (e.g. [56], [5], [29]) which have been developed rather separately so far. To that end, we first explain how convex optimization techniques [12], [41], [11] and, more precisely, ℓ_1- norm sparsity constraints affect the solution of such inverse problems as the deconvolution of sparse peaks (or point sources) on discrete grids (or meshes) when the convolution kernel is smooth (admissible) [8] and then we propose an adaptive super-resolution scheme. In particular, our contributions are two-fold and are summarized as follows:

1) Theoretical:

- With the help of the first order optimality condition of the ℓ_1-norm minimization problem, we show that the numerical solution consists of one or multiple peaks at grid points (or nodes) adjacent to the location of the actual peak. Our conclusions are inline with recent results presented in [29] for one dimensional spaces; but, the methodology employed, as well as the form in which the problems in question are expressed, are different. Previous approaches study the properties of the ℓ_1-norm numerical solution by introducing the extended computational support notion [29] or by deriving dual certificates that fulfils particular properties [64] which both were used nicely to obtain asymptotic properties of the signal support. Here, we take a step forward to characterize the values of the numerical solution on its support also in dependence of the exact peak locations. We use the optimality condition of the finite dimensional ℓ_1-norm minimization problem to investigate the conditions under which a single or multiple peaks are recovered in one dimensional spaces. Then, we define an optimality curve, directly related to

the optimality condition of the problem (respectively the dual certificate), whose shape allows us not only to justify the patterns of the expected numerical solutions on fixed computational grids both in one and higher dimensional spaces, but also infer further information on the location of the exact peaks.

- We show that we can explicitly approximate the locations and amplitudes of the exact peaks based on a set of linear equations derived from the associated normal equations of the ℓ_1-norm problem.

- We derive an a-posterior error between the original signal (I.2) and its discrete version (I.3) by employing the Bregman distance [42]. We show that the recovery error depends on the relative distance between the computational grid points and the locations of the original peaks.

2) Practical: The a-posterior error outcome and the numerical reconstructions of multiple peaks at grid points in the vicinity of the original peaks give us the intuition to introduce the adaptive grid concept for the recovery of the original peaks. Hence, we propose an adaptive super-resolution scheme consisting of two main stages. First we determine the intervals which include the support of the original peaks and we separate multiple original peaks which are close to each other. This is achieved by adjusting the grid as the computations proceed in a manner dependent upon the previous sparse solution. Then, the coordinates of the locations and the amplitudes of the peaks are approximated based on the numerical solution obtained from the first stage and the set of equations following from the optimality condition of the formed ℓ_1-norm minimization problem.

The proposed adaptive algorithm shares some similarities with other superresolution algorithms e.g. [55], [81]; however, our approach embeds an automatic adaptation scheme [77] since it restricts and refines the grid in an unsupervised manner only in the neighborhoods where there is indication that a peak exists. This additionally allows to solve iteratively a small to medium size linear problem using convex optimization techniques [12], instead of a big size problem as in [55].

Overall, our analysis provides theoretical insights on the effects of gridding (a.k.a discetization of the parameter space), and it can help the algorithmic development in the direction of avoiding heuristic post-processing steps by using information about the convolution kernel properties and the formulation of the minimization problem rather than resorting in unreliable approximations as often happens in application papers (e.g. in [74]).

II. DECONVOLUTION OF SPARSE PEAKS BY CONVEX OPTIMIZATION

In the following we discuss the theoretical basis of sparse peak deconvolution using convex optimization approaches and put it in perspective with classical discretization issues in numerical analysis.

A. Sparsity over the continuum and its discretization

Let us start by formulating the problem over the continuum, following [13], [27], which is the underlying ideal sparse peak deconvolution to which we expect minimizers of (I.5) to converge to. For a Radon measure μ on Ω we denote its total variation by

$$\|\mu\|_{TV} = \sup_{\varphi \in C_0(\Omega)} \int_{\Omega} \varphi(x) \, d\mu(x). \tag{II.1}$$

The convex variational problem solved for sparse peak deconvolution in a continuum setting is then given by

$$J_{\infty}(\mu) = \frac{1}{2}\|G * \mu - f\|^2 + \lambda\|\mu\|_{TV}. \tag{II.2}$$

Now (I.5) can be interpreted as a discretization on a given grid, it can indeed be rephrased as

$$J_N(\mu) = \begin{cases} \frac{1}{2}\|G * \mu - f\|^2 + \lambda\|\mu\|_{TV} & \text{if } \mu \in \text{ span}(\{\delta_{x_k}\}_{k=1,\dots,N}) \\ +\infty & \text{else.} \end{cases} \tag{II.3}$$

It is straight-forward to show that the functionals J_N Γ-converge to J_{∞}, but one can also ask for more quantitative error estimates, which we shall discuss below.

By standard arguments we can verify the following result for the discretized problem (cf. [14], [13], [27] for analogous results on the continuum problem (II.2)):

Proposition II.1. *For* $\lambda \geq 0$ *there exists a solution of* (I.5). *If* $\lambda > \|A^* f\|_{\infty}$ *then the unique minimizer is given by* $c = 0$. *If* $\lambda < \|A^* f\|_{\infty}$, *then each solution is different from zero.*

Proof. Convexity, coercivity, and nonnegativity immediately imply the existence of a minimizer.

Now let $\lambda > \|A^*f\|_\infty$, then

$$
\begin{aligned}
J(c) &= \frac{1}{2}\|Ac - f\|^2 + \lambda\|c\|_1 \\
&= \frac{1}{2}\|Ac\|^2 + \frac{1}{2}\|f\|^2 + \lambda\|c\|_1 - \langle A^*f, c \rangle \\
&\geq \frac{1}{2}\|Ac\|^2 + \frac{1}{2}\|f\|^2 + (\lambda - \|A^*f\|_\infty)\|c\|_1 \geq \frac{1}{2}\|f\|^2 \\
&= J(0),
\end{aligned}
$$

with inequality only for $c = 0$. Hence, $c = 0$ is the unique minimizer. In the case $\lambda < \|A^*f\|_\infty$ we choose $c = \epsilon A^*f$ with $\epsilon > 0$ sufficiently small to verify that there exists a c yielding a functional value lower than $\frac{1}{2}\|f\|^2$. $\qquad\square$

B. Optimality conditions

As a next step we state the optimality conditions for (II.2) and the discrete version (I.5). Those are important for error estimates and further analysis in this paper.

Let us start with the sub-differential of the total variation norm, which is given by (cf. [13])

$$
\partial\|\mu\|_{TV} = \{q \in L^\infty(\Omega) \mid \|q\|_\infty \leq 1, q(x) \equiv \pm 1 \text{ on } \text{supp}(\mu_\pm)\}. \tag{II.4}
$$

Here $\mu = \mu_+ - \mu_-$ denotes the standard Jordan decomposition of the signed measure μ. Since the quadratic part of the functional J_∞ is differentiable and G is continuous, i.e. the convolution maps into the pre-dual of the space of Radon measures, we obtain the optimality condition

$$
\|G * f - H * \mu\|_\infty \leq \lambda \tag{II.5}
$$

$$
G * f - H * \mu = \pm\lambda \quad \text{in } \text{supp}(\mu_\pm). \tag{II.6}
$$

where $H = G * G$. On the other hand, the optimality condition of the discrete problem (I.5) is

$$
\lambda p_j = [A^*(f - Ac)]_j \qquad \text{for } j = 1, \ldots, N, \tag{II.7}
$$

where $p \in \mathbb{R}^N$ is contained in the sub-differential of $\|c\|_1$. The right hand side of the previous equation[1] is $[A^T f]_j = \sum_{l=1}^L \gamma_l H(x_j - \xi_l)$ and $[A^T Ac]_j = \sum_{k=1}^N c_i H(x_j - x_k)$. The optimality

---

[1] The convolution of signal μ^N with a kernel, e.g. Gaussian G, is $G * \mu^N = \sum_{k=1}^N c_k G(x - x_k)$ and in matrix form this can be expressed as $[Ac]_j = \sum_{k=1}^N c_k G(x_j - x_k)$. Moreover, $G * G = H$ and since function G is symmetric and the convolution is associative $G * (G * \mu^N) = (G * G) * \mu^N = H * \mu^N = \sum_{k=1}^N c_k H(x - x_k)$.

condition can be written as

$$\lambda p_j = \sum_{l=1}^{L} \gamma_i H(x_j - \xi_l) - \sum_{k=1}^{N} c_k H(x_j - x_k), \qquad (\text{II.8})$$

for $k = j$, $p_j \in sign(c_j)$ when $c_j \neq 0$ and $|p_j| < 1$ when $c_j = 0$.

In order to highlight the connection with the continuum formulation, we rewrite the optimality solely for the measure μ^N and deduce that

$$G * f - |H * \mu^N| \leq \lambda \quad \text{in } \{x_k\}_{k=1,\dots,N} \qquad (\text{II.9})$$

$$G * f - H * \mu^N = \pm\lambda \quad \text{in supp}(\mu^N_{\pm}). \qquad (\text{II.10})$$

We see that the main difference to the optimality condition in the continuum is that the first equality only holds on the grid points x_k and not in the whole domain Ω. Note that due to the continuity of G and H one will expect (at least for sufficiently small grid size) that if $\frac{|H*\mu^N - G*f|}{\lambda} - 1$ is strictly less than zero in a set of neighbouring grid points, then it remain less than zero in the area bounded by these points (further details are given in section III-B2). Hence, the main violation of the continuum optimality condition considered for μ^N will appear close to grid points where it equals zero, usually corresponding to non-zero coefficients c_k. This yields a first idea for using an adaptive computational grid. As we shall see below this can be further improved and backed up by a-posteriori error estimation.

C. A-Posteriori error estimate

In order to derive suitable error estimates for non-smooth convex variational problems such as problem (I.5), it is now a standard approach to use the Bregman distance as proposed in [60] (we refer to [42] for an overview). The Bregman distance for the total variation distance is given by

$$D_{TV}^q(\tilde{\mu}, \mu) = \|\tilde{\mu}\|_{TV} - \|\mu\|_{TV} - \langle q, \tilde{\mu} - \mu \rangle \qquad (\text{II.11})$$

for a subgradient $q \in \partial \|\mu\|_{TV}$. Given a subgradient $\tilde{q} \in \partial \|\tilde{\mu}\|_{TV}$, we will denote by

$$D_{TV}^{\tilde{q},q} = D_{TV}^{\tilde{q}}(\mu, \tilde{\mu}) + D_{TV}^q(\tilde{\mu}, \mu) = \langle \tilde{q} - q, \tilde{\mu} - \mu \rangle \qquad (\text{II.12})$$

the symmetric Bregman distance.

The key idea here is to use the difference in the optimality conditions and take a duality product with the difference of the measures. For this sake, we use the following notation

$$
\begin{aligned}
q^N(x) &:= \min\{\max\{\frac{G * f(x) - H * \mu^N(x)}{\lambda}, -1\}, 1\}, \\
r^N(x) &:= \frac{G * f(x) - H * \mu^N(x)}{\lambda} - q^N(x).
\end{aligned}
\tag{II.13}
$$

It is straightforward to see that $q^N \in \partial \|\mu^N(x)\|_{TV}$ and hence from (II.5), (II.9) and (II.13) we obtain

$$
H * (\mu - \mu^N) + \lambda(q - q^N) = \lambda r^N.
\tag{II.14}
$$

Now the announced duality product with $\mu - \mu^N$ implies an a-posterior error estimate of the form

$$
\|G * (\mu - \mu^N)\|^2 + \lambda D_{TV}^{q,q^N}(\mu, \mu^N) = \lambda\langle r^N, \mu - \mu^N\rangle.
\tag{II.15}
$$

Thus, we observe that only regions with $r^N \neq 0$ contribute to the error between μ and μ^N.

Moreover, via the optimality condition (II.9) of problem (I.5), we have that $r^N(x_k) = 0$ for any grid point x_k and thus $\langle r^N, \mu^N\rangle = 0$. So, we can write

$$
\|G * (\mu - \mu^N)\|^2 + \lambda D_{TV}^{q,q^N}(\mu, \mu^N) \leq \lambda\|r^N\|_\infty \|\mu\|_{TV}.
\tag{II.16}
$$

The previous expression shows that by reducing the supremum norm of r^N is crucial for reducing the global error. This can be achieved by introducing finer computational grids. In Figure 1 we can observe that the value of $\|r^N\|_\infty$ decreases with respect to the size of the computational grid. However, we remark that by introducing fixed fine grids (as proposed for instance in [81], [57], [55]) the computational performance and stability can be affected. To overcome computational limitations, we later propose to introduce a progressive grid refinement.

III. NUMERICAL SOLUTIONS IN THE CASES OF SINGLE PEAKS

Here, as started in [39] we analyze in detail the solutions of the form (I.3) in the case of noiseless data f produced by a single positive peak, i.e.

$$
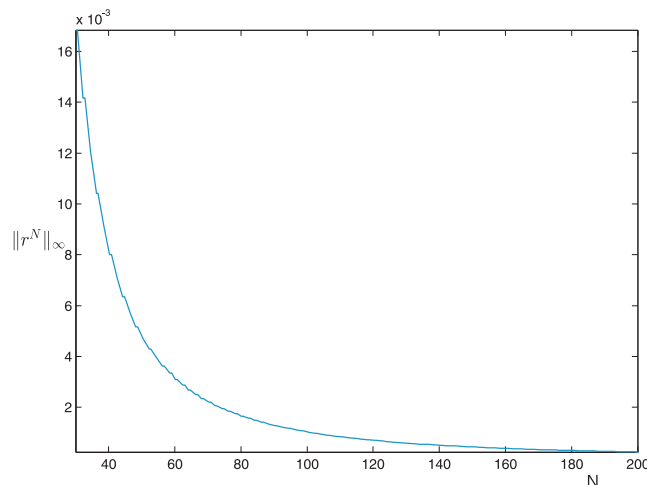\mu = \gamma \delta_\xi, \qquad \text{and} \qquad f(x) = \gamma G(x - \xi),
\tag{III.1}
$$

Fig. 1: Supremum norm of r^N(residual) with respect to the size N of the computational grid. Here, we considered $\mu = \delta_\xi$ and $\mu^N = \sum_{k=1}^{N} c_k \delta_{x_k}$. Thus, $r^N(x) = \frac{H(x-\xi)-\sum_{k=1}^{N} c_k H(x-x_k)}{\lambda} - q^N(x)$ based on (II.13) and $H(x)$ was a Gaussian kernel.

where $\xi \in \mathbb{R}^d$ and $d \geq 1$ [2]. We can easily interpret Proposition (II.1) in this case as $A^* f = \gamma[H(x_j - \xi)]_{j=1,\dots,N}$ and $\|A^* f\|_\infty > \lambda$ in order to obtain nonzero solutions. Hence, we need $\lambda < \gamma \max_j \{H(x_j - \xi)\}$ and since H attains its maximum at zero, a simple sufficient condition is given by

$$\lambda < \gamma H(0), \tag{III.2}$$

which is also necessary in the case of ξ coinciding with a grid point. We will thus assume condition (III.2) throughout the whole section without further notice.

A. Exact recovery

The simplest case to start with, which can directly be treated in arbitrary dimensions, is that ξ coincides with one of the grid points. In this case we obviously expect perfect reconstruction, which is confirmed by the following result:

Proposition III.1. *Let be $\xi = x_K$ for some $K \in \{1, \dots, N\}$. Then there exists a one-sparse solution μ^N of (I.5), which is nonzero at x_K, i.e., $\mu^N = c_K \delta_{x_K}$ with $c_K = \frac{\gamma H(0)-\lambda}{H(0)} \in (0, \gamma)$.*

---

[2]Our analysis is based on a single positive peak which is often the case in image processing applications. We note that the theorems/conclusions presented in this section are valid also for a negative peak.

Proof. Without restriction of generality assume that $\gamma > 0$. In order to prove the assertion, we have to check whether the optimality condition of (I.5) holds under the assumptions mentioned above. From our prior computations (II.8), the optimality condition (II.8) reduces to

$$\lambda p_j = \gamma H(x_j - \xi) - c_K H(x_j - x_K) = (\gamma - c_K) H(x_j - x_K). \tag{III.3}$$

We have to differentiate between the cases where $j = K$ and $j \neq K$.

For $j = K$ the optimality condition (III.3) is

$$p_K = (\gamma - c_K)\frac{H(0)}{\lambda} = 1 \,. \tag{III.4}$$

For $j \neq K$ we have

$$p_j = \frac{\gamma - c_K}{\lambda} H(x_j - x_K) < (\gamma - c_K)\frac{H(0)}{\lambda} \,,$$

due to the fact that H attains its maximum at zero. Hence in both cases the optimality condition is fulfilled and we obtain the assertion. $\qquad\square$

Therefore, the reconstruction of the support of a delta peak is exact if the position of the peak coincides with a grid point and the regularization parameter is small enough.

B. Recoveries for off-the-grid peaks

Let us consider the more frequent case where $\mu = \gamma\delta_\xi$ is located among a set of grid points $\mathcal{N} = \{x_k\}_{k=1:N}$. Here, with the help of the optimality conditions (II.9), we define a so-called optimality curve $p(x)$ given by

$$p(x) = \frac{G * f - H * \mu^N}{\lambda} - 1, \tag{III.5}$$

where $f = G * \mu$, $H = G * G$ (smooth and symmetric) and $\mu^N = \sum_{x_k \in \mathcal{N}} c_k \delta_{x_k}$ is the nontrivial numerical solution obtained from the minimization problem (I.5). The optimality curve $p(x)$ can be regarded as analogous to the TV dual certificate [65] for the ℓ_1- norm minimization problem that will allow us to understand the expected patterns of the numerical solutions around ξ.

To ease our analysis, we rewrite $p(x)$ as

$$p(x) = \frac{1}{\lambda}H(x - \xi) - \frac{1}{\lambda}\sum_{x_k \in \mathcal{N}} c_k H(x - x_k) - 1. \tag{III.6}$$

We note that $p(x_j) < 0$ when $c_j = 0$ and $p(x_j) = 0$ when $c_j > 0$.

1) Single spatial dimension: In one dimensional spaces, we consider that signal $\mu = \gamma\delta_\xi$ is located between two grid points, i.e. $\xi \in (x_K, x_{K+1})$. For the following consideration, the interval length h will be defined as

$$h := |x_{K+1} - x_K| \ .$$

By employing function $p(x)$ (III.6) in the vicinity of peak ξ, we can prove the following Theorem.

Theorem III.2.

Let $H \in C^3(\mathbb{R})$ be nonnegative with a unique maximum at zero and let h be sufficiently small. Assume $\mu = \gamma\delta_\xi$, $\xi \in (x_K, x_K + \frac{h}{2})$ for $K \in \{1, \ldots, N-1\}$ and $\lambda < \gamma H(x_K - \xi)$ holds.

When we have that $\xi \in (x_K, x_K + \frac{\lambda h}{2\gamma H(0)})$, there exists a solution of (I.5), which can be written as $\mu^N = a\delta_{x_K}$ with $a = \frac{\gamma H(x_K - \xi) - \lambda}{H(0)} \in (0, \gamma)$.

Moreover, if we have $\xi \in (x_K + \frac{\lambda h}{2\gamma H(0)}, x_K + \frac{h}{2})$, then $\mu^N = a\delta_{x_K}$ is not a solution of (I.5) for any $a \in \mathbb{R}^+$. Instead the solution is of the form $\mu^N = c_K\delta_{x_K} + c_{K+1}\delta_{x_{K+1}}$ with c_K and c_{K+1} being nonzero and of the same sign as γ.

The proof of Theorem III.2 is given in Appendix A. Figure 2 illustrates the assertion of Theorem III.2. Note that due to the symmetry of H, the analogous claim holds for ξ in the other half of the interval. Figure 3 depicts the optimality curve $p(x)$ for a positive peak when $H(x)$ is a Gaussian
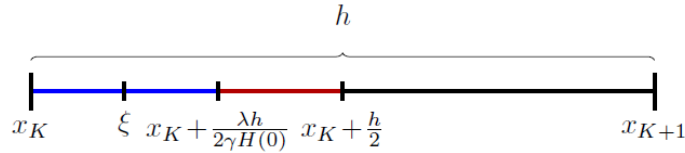

Fig. 2: If ξ is in the blue interval, the reconstructed solution μ^N consists of only one peak. In the case that ξ is located in the red interval, then one recovered peak is not sufficient.

kernel. The curve is downward concave in the area around ξ which implies that there are at most two points on x-axis where $p(x) = 0$. From these points, at least one is the grid point with the nonzero coefficient of μ^N. We can observe that the number of the recovered peaks depends on the distance between the location of the exact peak (denoted by red x) and the neighboring grid points (given fixed $\lambda = 0.1\lambda_{\max}$).
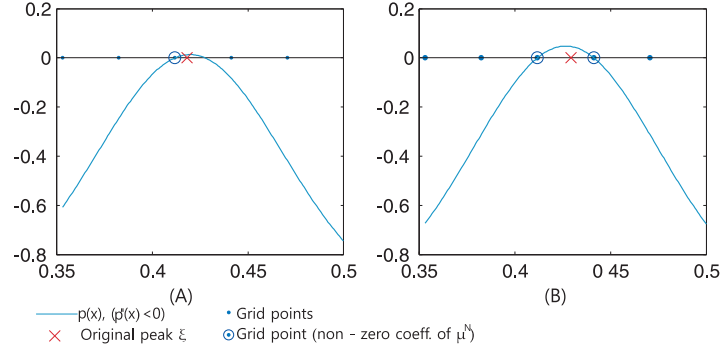
Fig. 3: Function $p(x)$ around location ξ for the cases where the reconstructed signal μ^N has (A) a single nonzero coefficient and (B) two nonzero coefficients between the location of the exact peak ξ.

2) Higher spatial dimension: In higher spatial dimensions, the topological structure is more complicated which makes a rigorous proof by analogous arguments impossible. However, we can at least make some formal arguments and computational experiments concerning the optimality curve $p(x)$ (III.6). First of all we expect that for $\gamma > 0$, $p(x)$ is concave around ξ and nonzero entries are only found in the convex hull of ξ on the grid, i.e. the largest convex hull C_ξ that can be formed of a set of grid points surrounding the peak ξ such that no other grid point is contained in C_ξ.

The following observations can be made:

- Given any location x far from ξ, we have that $p(x) < 0$, since the positive term $H(x - \xi)$ is smaller than $H(x - x_k)$.

- Since the kernel $H(x)$ is smooth, and considering that its width is greater than the resolution of the selected grid (which is often the case for low resolution images), then $p(x) < 0$ in the area bounded by grid points where $c_j = 0$.

- Given $\{x_j \mid c_j > 0\}$ forms a small neighborhood of ξ, consisting of $N \geq 1$ points, we can make a local Taylor expansion similar to the one-dimensional case. First of all we have that $p(x_j) = 0$ for all such j. By summing those with respect to j we get

$$\sum_j \sum_k c_k H(x_j - x_k) = \sum_j H(x_j - \xi) - \lambda N .$$

Using the lowest order approximation for small arguments we find

$$NH(0) \sum_k c_k = NH(0) - \lambda N + \mathcal{O}(h^2) \,,$$

i.e. to first order

$$\sum_k c_k = 1 - \frac{\lambda}{H(0)} \tag{III.7}$$

Using this approximation the Hessian can be computed to leading order as

$$\nabla\nabla p(\xi) = \frac{1}{\lambda} H(0) - \frac{1}{\lambda} \sum_j c_j H(\xi - x_j) - 1 \tag{III.8}$$

$$= \nabla\nabla H(0) \,, \tag{III.9}$$

which is negative definite due to our assumptions on H. Hence, p is concave in a neighbourhood of ξ, which implies that its level sets are convex. The points x_j with $p(x_j) = 0$ are on the level set $\{p = 0\}$, i.e. a convex set around ξ. Since $p(x_k) > 0$ is impossible, there is no other grid point inside the convex hull of the $\{x_j\}$.

Thus, from those arguments we see that the active grid points ($c_j > 0$) are to be expected in the convex hull of ξ on the grid. This can be made rigorous under the assumption that the local grid size around ξ is small and there are no active grid points at large distance from ξ, which is confirmed in all our numerical experiments. Figure 4 illustrates this behaviour by showing the shape of the function p and its relationship to the nonzero coefficients of the reconstructed signal μ^N. In this figure, the small blue dots depict the computational grid, the big blue circles show the grid points with nonzero entries (i.e. estimated peaks). For the computations, the regularization parameter was set $\lambda = 0.1\lambda_{\max}$ and $H(x)$ was Gaussian with standard deviation $\sigma = 1.5\sqrt{2}h$ (where h was the grid resolution). Based on the previous analysis, we can see in Figure 5 that the numerical solution depends on λ and the properties of kernel H. As expected, the number of active grid points increases as λ decreases which is effectively a property of the finite-dimensional ℓ_1-norm regularization in the convex hull on the grid.

IV. RECOVERIES OF SINGLE PEAKS USING THE ℓ_1-NORM OPTIMALITY CONDITION

Let the observations f be of the form $f(x) = \gamma G(x - \xi) + \tilde{f}$, with $\tilde{f}$ supported in some distance to ξ. Then, we expect that problem (I.5) will yield few nonzero coefficients $\{c_k\}$ only in
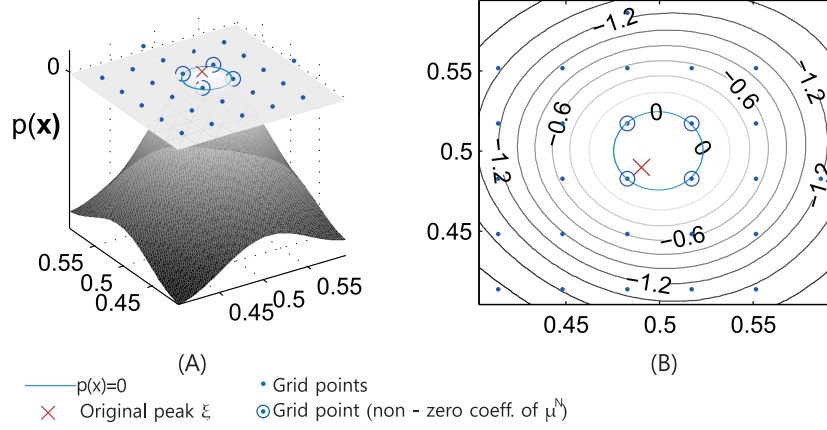
Fig. 4: Function $p(x)$ around location ξ when the reconstructed signal μ^N has four nonzero coefficients. (A) 3D plot of $p(x)$ and xy-plane with the computational grid (marked blue dots) and location of the nonzero coefficients (marked with blue circles) (B) Isocontours of $p(x)$, computational grid (marked with blue dots) and nonzero locations of μ^N (marked with blue circles). The exact location denoted by red x.
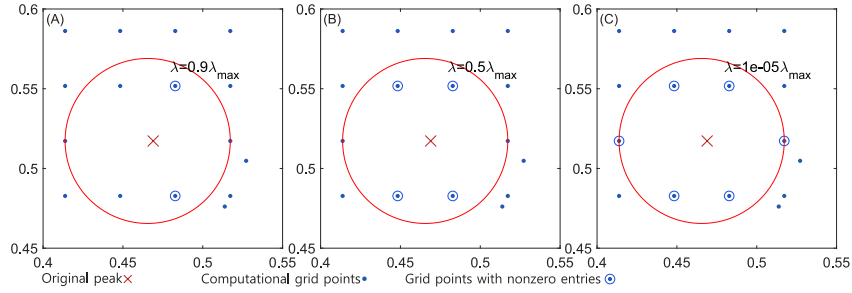

Fig. 5: Numerical solution on a grid for decreasing value of the regularization parameter λ. The blue circles show the locations of the nonzero coefficients of the numerical solution. The blue dots are the grid points. The red circle is the smallest circle that encloses the largest convex hull formed by grid points that surround ξ (points that can get nonzero entries). The maximum number of nonzero entries is depicted in (C).

a neighborhood of grid points, $\mathcal{N} = \{x_k\}$, close to ξ plus additional non-zeros related to $\tilde{f}$ in a certain distance. Hence, the confined variational problem is

$$\min_{(c_k)_{x_k \in \mathcal{N}}} \| \sum_{x_k \in \mathcal{N}} c_k G * \delta_{x_k} - f \|^2 + \lambda \sum_{x_k \in \mathcal{N}} |c_k| \, ,$$

where all the c_k have same sign $s \in \{+1, -1\}$.

The associated normal equations are

$$\sum_{x_k \in \mathcal{N}} c_k G * G(x_i - x_k) - G * f(x_i) + \lambda s = 0 \ , \tag{IV.1}$$

for $x_i \in \mathcal{N}$ (note that s is the same for all x_i). Given $H(x) = G * G(x) = \int_\Omega G(x - y)G(y) \ dy$, we can write the associated normal equations as

$$\sum_{x_k \in \mathcal{N}} c_k H(x_i - x_k) - \gamma H(x_i - \xi) + \lambda s = (G * \tilde{f})(x_i) \text{ for } x_i \in \mathcal{N}. \tag{IV.2}$$

For a small neighbourhood around ξ (and $h \to 0$ a bound for the grid size) we can perform a Taylor-expansion and obtain

$$\left(\sum_{x_k \in \mathcal{N}} c_k - \gamma \right) H(0) + \frac{1}{2} \sum_{x_k \in \mathcal{N}} c_k (x_i - x_k)^T \nabla^2 H(0)(x_i - x_k) - \frac{1}{2}\gamma(x_i - \xi)^T \nabla^2 H(0)(x_i - \xi) + \lambda s$$

$$= (G * \tilde{f})(\xi) + \nabla(G * \tilde{f})(\xi)(x_i - \xi) + \frac{1}{2}(x_i - \xi)^T \nabla^2(G * \tilde{f})(\xi)(x_i - \xi) + \mathcal{O}(h^3) \ , \tag{IV.3}$$

where we have used $\nabla H(0) = 0$. We observe that all equations have the same leading order term, which yields up to order two

$$\gamma = \sum_{x_k \in \mathcal{N}} c_k + \frac{\lambda s}{H(0)} - \frac{(G * \tilde{f})(\xi)}{H(0)} \ . \tag{IV.4}$$

In order to access higher-order terms we can exploit the fact that set $\mathcal{N}$ of nonzero coefficients has more than one grid point and thus we can estimate differences of equation (IV.3) for pairs of grid points $x_i, x_j \in \mathcal{N}$. This yields

$$\begin{aligned} \gamma(x_i - x_j)^T \nabla^2 H(0)\xi = &\frac{\gamma}{2} \left(x_i^T \nabla^2 H(0)x_i - x_j^T \nabla^2 H(0)x_j \right) \\ &- \frac{1}{2} \sum_{x_k \in \mathcal{N}} c_k \left(F_k(x_i) - F_k(x_j) \right) \\ &+ \frac{1}{2}\tilde{F}(\xi) + \mathcal{O}(h^3) \end{aligned} \tag{IV.5}$$

where $F_k(x) = (x - x_k)^T \nabla^2 H(0)(x - x_k)$ and $\tilde{F}(\xi) = (x_i - \xi)^T \nabla^2(G * \tilde{f})(\xi)(x_i - \xi) - (x_j - \xi)^T \nabla^2(G * \tilde{f})(\xi)(x_j - \xi) + \nabla(G * \tilde{f})(\xi)(x_i - x_j)$. Equation (IV.5) can be interpreted as a linear equation for $\xi \in \Omega$. Having at least $m > d$ different grid points in $\mathcal{N}$, we can derive $m(m - 1)/2$ equations. . If we can choose the $x_i - x_j$ to be a basis of $\mathbb{R}^d$, the negative definiteness of $\nabla^2 H(0)$

and $\gamma \neq 0$ imply that the matrix formed out of the vectors $\gamma(x_i - x_j)^T \nabla^2 H(0)$ has rank d. Thus, we can uniquely solve for the location ξ and obtain a second order approximation in h (considering the contribution from $\tilde{f}$ negligible).

A. Examples of peak recoveries

To demonstrate the previous theoretical results, we present some examples in one and two dimensional spaces.

1) 1D spaces: In the following examples, we consider a signal with three peaks with amplitudes γ_1, γ_2 and γ_3 at positions ξ_1, ξ_2 and ξ_3 where $\xi_l \in (0, 1)$ for $l = 1, 2, 3$. The signal is given by

$$\mu = \gamma_1 \delta_{\xi_1} + \gamma_2 \delta_{\xi_2} + \gamma_3 \delta_{\xi_3} .$$

Moreover, we choose a Gaussian convolution kernel G with standard deviation $\sigma = 0.03$. The continuous convolved data can be expressed analytically as

$$f(x) = \gamma_1 G(x - \xi_1) + \gamma_2 G(x - \xi_2) + \gamma_3 G(x - \xi_3) .$$

For the estimation of the numerical solution μ^N the domain $[0, 1]$ is discretized and the ℓ_1-norm minimization problem (I.5) is solved with $\lambda = 0.01\|A^* f\|_\infty$ on a uniform grid of size N.

We first consider a grid that includes ξ_1, ξ_2 and ξ_3. In Figure 6, we observe that the exact recovery is feasible (which is in accordance with preposition (III.1)).

Now we can consider the case of Theorem III.2 where the three peaks of μ are located between the grid points. Figure 7 and 8 depict the results for two different grids of size $N = 16$ and $N = 51$ respectively. The numerical solutions yield to either two peaks around the location of an original peak or a single peak close to the original one as one expects.

To approximate the amplitude and location of the underlying peaks we used equation (IV.4) and (IV.5) respectively. In particular, for the approximation of a peak located at $\xi_l \in (x_k, x_{k+1})$ with amplitude γ_l, if there exist two nonzero coefficients c_k and c_{k+1} at points x_k and x_{k+1} respectively, then from (IV.4) follows that

$$\hat{\gamma}_l = c_k + c_{k+1} + \frac{\lambda\, s}{H(0)} , \qquad (IV.6)$$

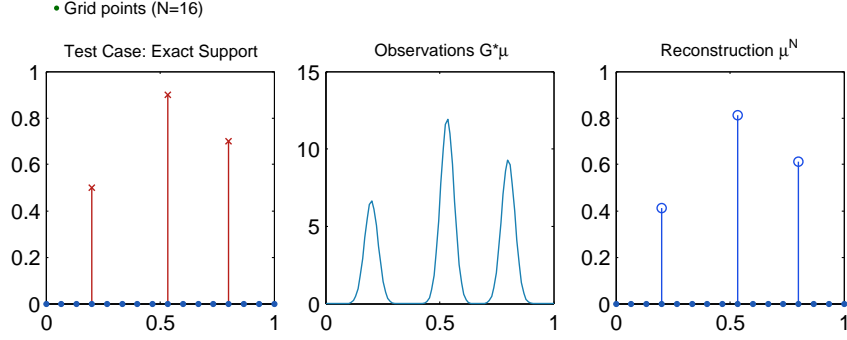If $c_k > 0$ and $c_{k+1} > 0$, $s = 1$.

Fig. 6: Left image: Original peaks, middle image: observations and right image: solution of the discrete convex problem (I.5). The solution of the ℓ_1-norm minimization problem for a computational grid which includes points ξ_1, ξ_2 and ξ_3 enables the exact recovery of the peak positions. The peaks of μ are at locations $\xi_1 = 0.2$, $\xi_2 = 0.533$ and $\xi_3 = 0.8$ and their amplitudes are $\gamma_1 = 0.5$, $\gamma_2 = 0.9$ and $\gamma_3 = 0.7$ respectively. The number of grid points used here was $N = 16$ ($h = 0.1$).

Based on equation (IV.5), the peak location is approximated as

$$\hat{\xi}_l = \frac{1}{2}(x_k + x_{k+1}) + \frac{c_{k+1} - c_k}{2\hat{\gamma}_l}(x_{k+1} - x_k) \ . \tag{IV.7}$$

Terms that include $(G * \tilde{f})$ in equation (IV.4) and (IV.5) has been eliminated from (IV.6) and (IV.7) since we use only the neighboring point contributions to recover the amplitude and position of the underlying peaks.

We note that in the case where the numerical solution yields to a single nonzero coefficient c_k at x_k, then $\hat{\gamma}_l = c_k$ and $\hat{\xi}_l = x_k$. Table I summarizes the values of the amplitudes and locations of the original and estimated peaks for the two different computational grids of Figure 7 and 8. Based on these results, the reconstructions in a fine grid are slightly more accurate than ones obtained using a coarse grid, which is inline with the a-posteriori error analysis presented in section II-C.

2) 2D spaces: In higher dimensions, the exact signal is $\mu = \sum_{l=1}^{L} \gamma_l \delta_{\xi_l}$ where $\xi_l \in \Omega \subset \mathbb{R}^d$ $(d > 1)$ and the estimated μ^N solution has nonzero values clustered in grid points around the locations of the actual peaks ξ_l. If a cluster of grid points with nonzero coefficients around peak ξ_l is denoted by $\mathcal{N}_l = \{x_k\}_{1:N_l}$, we approximate the peak amplitude according to

$$\hat{\gamma}_l = \sum_{x_k \in \mathcal{N}_l} c_k + \frac{\lambda s}{H(0)} \ . \tag{IV.8}$$
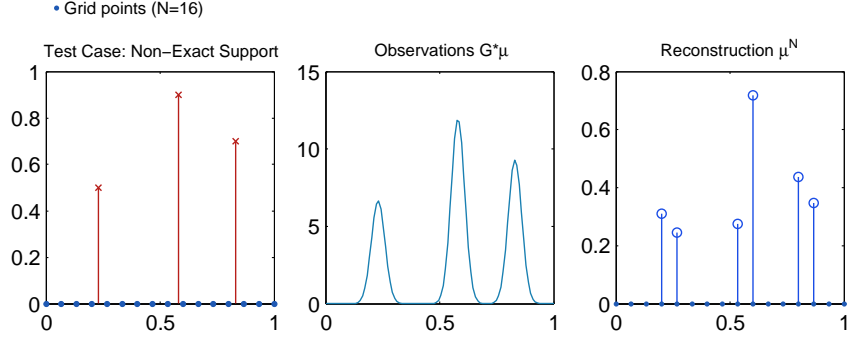
Fig. 7: Left image: Original peaks, middle image: observations and right image: solution of the discrete convex problem (I.5). The solution of the ℓ_1-norm minimization problem for a computation grid which does not include points ξ_1, ξ_2 and ξ_3 gives, as a solution, pairs of peaks adjacent to location of the original peak.
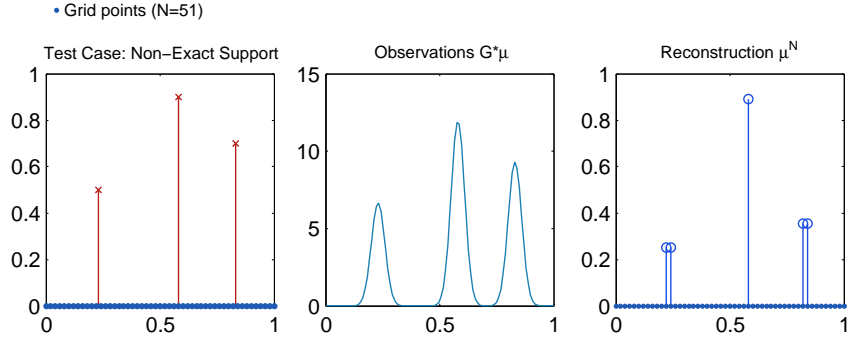

Fig. 8: Similar as Figure 7, however finer grid is used in the computation. The solution yields two pairs of peaks around ξ_1 and ξ_3 and a single peak close to ξ_2

True		N=16		N=51	
ξ	γ	$\hat{\xi}$	$\hat{\gamma}$	$\hat{\xi}$	$\hat{\gamma}$
0.23	0.5	0.2312	0.55	0.2301	0.50
0.58	0.9	0.5751	0.92	0.5800	0.91
0.83	0.7	0.8312	0.77	0.8300	0.71

TABLE I: This table summarizes the results of the test cases illustrated in Fig. 7 and Fig 8. The first and second column show the locations ξ and amplitudes γ of the underlying peaks, then there are the estimated locations and amplitudes for the cases where a coarse grid (N=16 points) and a fine grid (N=51 points) were used.

The location is approximated similarly as in (IV.5). Particularly, if there are at least two grid points x_i and $x_j \in \mathcal{N}_l$, we have

$$
\hat{\gamma}_l(x_i - x_j)^{\mathrm{T}} \nabla^2 H(0)\hat{\xi}_l = \frac{\hat{\gamma}_l}{2} \left(x_i^{\mathrm{T}} \nabla^2 H(0)x_i - x_j^{\mathrm{T}} \nabla^2 H(0)x_j \right)
$$
$$
- \frac{1}{2} \sum_{x_k \in \mathcal{N}_l} c_k \left(F(x_i) - F(x_j) \right), \tag{IV.9}
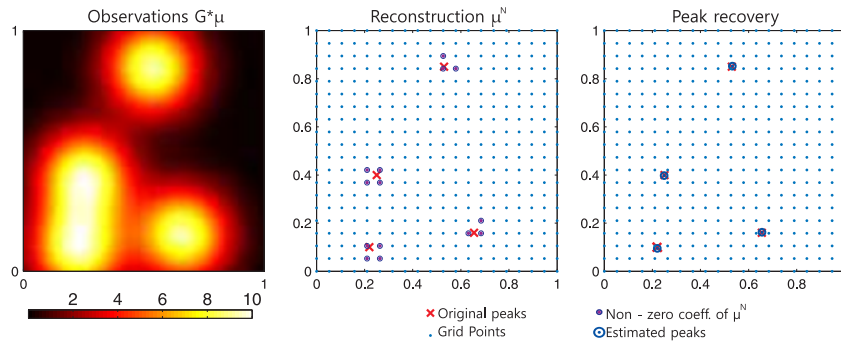$$

Fig. 9: Left image: Observations (convolution with a Gaussian kernel with standard deviation 0.13), middle image: numerical solution μ^N estimated solving the finite dimensional ℓ_1-norm problem (with $\lambda = 0.001\lambda_{\max}$) on a uniform grid 20×20, and right image: approximation of the peak locations using the clusters of nonzero coefficients obtained from ℓ_1-norm minimization.

where $F(x) = (x - x_k)^{\mathrm{T}}\nabla^2 H(0)(x - x_k)$. Having $N_l > d$ different grid points in $\mathcal{N}_l$, we can approximate the location of ξ_l solving a set of equations (IV.9) which are constructed by selecting one x_i at a time and taking differences to all other $x_j \in \mathcal{N}_l$.

As an example here we have a low resolution image produced as the convolution of four peaks with a Gaussian kernel in a two dimensional space. The domain is $\Omega = [0,1]^2$ (left image of Figure 9) and the selected computational grid is of size $N = 20 \times 20$ (depicted as small blue dots in the middle and right images of Figure 9). The middle image of Figure 9 shows the numerical result obtained solving the ℓ_1-norm minimization problem. The intense blue circles illustrate the locations where nonzero entries appeared. We can observe that there are four distinctive clusters of grid points with nonzero coefficients.

Therefore, four peaks are approximated, one for each cluster using (IV.9). The peak approximations are shown in the right image of Figure 9. Table II summarizes the results of the numerical solution μ^N and the corresponding approximate peaks $(\hat{\gamma}, \hat{\xi})$.

Location		Amplitude	
ξ	$\hat{\xi}$	γ	$\hat{\gamma}$
(0.22,0.10)	(0.2204,0.0950)	1	0.99
(0.66,0.16)	(0.6557,0.1620)	1	1.10
(0.53,0.85)	(0.5323,0.8525)	1	1.02
(0.25,0.40)	(0.2487,0.3977)	1	1.11

TABLE II: Locations, ξ, and $\hat{\xi}$ and amplitudes, γ and $\hat{\gamma}$ of the original and estimated peaks respectively for the case presented in Figure 9.

V. RECOVERIES IN THE CASE OF MULTIPLE PEAK SIGNALS

A coarse computational grid, even though reduces the computational cost, imposes some limitations to detect and separate neighbouring peaks. For example, there is always a possibility that there are more than one positive peak in an interval between two grid points (see one dimensional example of Figure 10.A), or two or more original peaks may be located in adjacent intervals (e.g. Figure 10.B). Then the numerical solution μ^N of the ℓ_1-norm minimization problem may not be accurate enough.

Following similar analysis as in Theorem (III.2), we can easily show that there exists a ℓ_1-norm solution $\mu^N = a\delta_{x_k}$ with $a = \frac{\sum_{l=1}^{L} \gamma_l H(x_k - \xi_l) - \lambda}{H(0)}$ as depicted in Figure 10.A even though the original peaks are two. Additionally, when the original peaks are distributed between two intervals then we can expect up to three reconstructed peaks as in Figure 10.B and Figure 10.C. A natural way
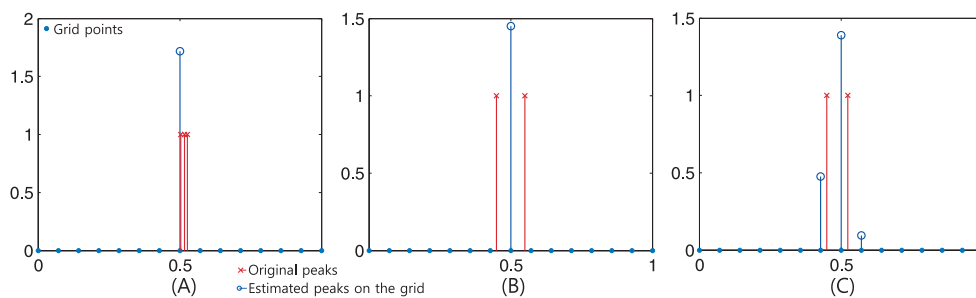

Fig. 10: In this figure, we show the peak recovered when there are more than one original peaks. (A) A single peak reconstruction (in blue) when the original peaks (in red) are very close to a grid point x_k (B) A single peak reconstruction (in blue) when the original peaks (in red) are symmetrically located with respect to a grid point. (C) Three peak reconstruction (in blue) when there are two original peaks (in red) on adjacent intervals.

to improve the estimates is by refining the grid. Figure 11 illustrates how by performing local refinements on the grid (and fitting the input data with a solution in the updated grid), we can achieve a separation of the underlying peaks.

A. Adaptive super-resolution for sparse signal

1) Overview: In the following context, to ease our analysis and to proceed with the domain refinement in higher dimensions instead of using grid/points we use the mesh/nodes notion as in the finite element methods. Hence, the computational domain can be described by a mesh consisting of a set of nodes (equivalent to grid points) and elements (e.g. line segments in one dimension or
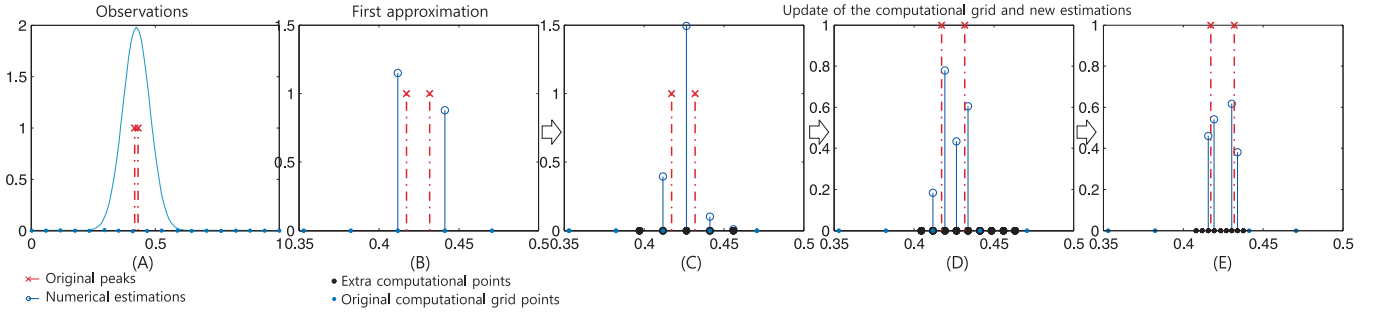
Fig. 11: By restricting and refining iteratively the computational grid around the nonzero coefficients of the numerical solution μ^N , we can determine small disjoint intervals where the two original peaks (in red) belong to and thus separate them. Fig.(A) shows the observations, original peaks (in red) and the locations of the used computational grid (small blue dots). Fig.(B)-(E) illustrate the reconstructed peaks (in blue) on a grid that is updated based on the previous numerical solution.

triangles in two dimensions). The proposed super-resolution approach consisting of the following steps:

   a)   Solve the ℓ_1-norm minimization problem (I.5) on a set of given nodes using a non-smooth convex solver;

   b)   Define a new (restricted) computational domain using the nodes (locations) corresponding to the nonzero coefficients of the estimated numerical solution (I.3). To do that:

      1) Remove the elements where all their nodes are assigned to zero coefficients; Cluster all the remaining elements. A cluster is defined by a set of pairwise connected elements (elements that share an edge or surface);

      2) Refine the computational domain at the estimated clusters by including extra nodes (i.e. centroids of the elements). Include only the extra nodes that satisfy a distance limit from the existing nodes.

      3) For each cluster, use the old and additional nodes to produce a mesh. The new (fragmented) computational domain consisting of all the disjoint clusters;

   c)   Repeat step a-b until domain stops updating i.e. the distance between the existing and additional nodes becomes sufficiently small[3];

   d)   Based on the last numerical solution (step c), for each separate cluster, estimate a single peak i.e. amplitude (IV.8) and location using the coordinates of the nodes corresponding

---

[3]For example, determine a minimum distance for the nodes using limits presented in [64], [65] or prior information about the size of the compressible signal.

to the nonzero coefficients of the numerical solution and the set of equations stemming from equation (IV.9).

A more analytical description of the approach is given in Appendix B. We need to mention that the proposed scheme is applicable for peaks of similar sign or when the positive and negative peaks satisfy the separation criteria (which is based on the kernel's width and noise type/level) as studied in some cases for example in [29], [64].

VI. RESULTS AND DISCUSSION

To demonstrate how the proposed superresolution approch can be used, we reconstruct super-resolved images from (low resolution) observations which are the convolution of an original sequence of sparse Dirac delta functions with Gaussian kernels. In this section, we present technical details about the simulated data, the proposed super-resolution approach and the validation metrics used for the comparison between the original peaks and the estimated ones. Then, we show examples how the proposed scheme progressively localizes a different number of peaks, which can be either only positive or positive and negative. Finally, we discuss further extensions and possible applications.

A. Simulated data

The simulations were carried out in a two dimensional square domain $\Omega = [0,1]^2$. The aim was to approximate the locations and amplitudes of an original signal $\mu = \sum_{l=1}^{L} \gamma_l \delta_{\xi_l}$ from low resolution images $W \in \mathbb{R}^{M \times M}$ where

$$w_{j_1 j_2} = \sum_{l=1}^{L} \gamma_l G(\xi_l - x_{j_1 j_2}) + \varepsilon_{j_1 j_2} \,,$$

for $j_1, j_2 = 1, \ldots, M$ (where $\xi_l \neq x_{j_1 j_2} \forall j_1, j_2$).

As a convolution kernel, we use the one from study [55], given by

$$G(x) \propto \alpha \exp\left(\frac{1}{2}\left(x^{\mathrm{T}} \Gamma_1^{-1} x\right)\right) + (1-\alpha) \exp\left(\frac{1}{2}\left(x^{\mathrm{T}} \Gamma_2^{-1} x\right)\right) \,,$$

with $\alpha = 0.2$, covariance matrices $\Gamma_1 = \sigma_i I^{2 \times 2}$, $\Gamma_2 = \sigma_2 I^{2 \times 2}$, $\sigma_1 = 2\ h_M$, $\sigma_2 = 2.5 h_M$ and $h_M = 1/M$.

Also, we considered a low additive measurement noise $\varepsilon = \mathrm{sc}\ \bar{\varepsilon} \in \mathbb{R}^{M \times M}$ where $\bar{\varepsilon} \in \mathbb{R}^{M \times M}$ was sampled from a Gaussian distribution with zero mean and variance one. The scaling parameter sc

was estimated based on the level of the signal-to-noise ratio (SNR), $\text{SNR} = 10 \log_{10} \frac{\sum_{j_1,j_2=1}^{M} (\sum_{l=1}^{L} \gamma_l G(\xi_l - x_{j_1 j_2}))^2}{\sum_{j_1,j_2=1}^{M} (\varepsilon_{j_1 j_2})^2}$. In the following simulations, we used $\text{SNR} = 40$ dB.

B. Details about the adaptive superresolution approach

We estimated the locations and the amplitudes of the underlying peaks by employing the proposed scheme of section V. The initial estimation (by solving the ℓ_1-norm minimization) was performed in a uniform mesh of $N \times N$ nodes. Then, the mesh was updated automatically around the nonzero entries of vector c. In practice, to avoid small numerical inaccuracies, the new domain was defined by keeping the nodes with absolute values of the estimated peaks greater than a small threshold (i.e. 0.5% of the maximum $|c|$ of vector c). In the current implementations, the ℓ_1-norm minimization problem was solved using the hierarchical adaptive lasso (HAL) [58]. Other algorithms e.g.[10], [48] could be used as well. Here, we used HAL to reduce the amplitude shrinkage of the estimated nonzero coefficient given a regularization parameter λ. In the following examples, $\lambda = 0.1\lambda_{\max}$. Moreover, the incorporation of a Bregman iteration [80] could be considered in the future for cases with relative high measurement noise.

The updates of the computational support terminated when the distance between the existing nodes and the additional nodes became small. In the following examples, we used as a criterion for adding a new node, the minimum distance of this candidate node from the existing nodes, $h_{\min} = 0.25 h_M$ (approximately 0.125 of the Gaussian kernel's standard deviation). This choice was made to enable a computational efficiency (i.e. a reasonable number of iterations) and to allow a good approximation of the peaks using small clusters of the nonzero coefficients and (IV.9).

C. Comparison metrics

In tests with only few peaks, we used:

- The mean localization error (MLE) between the original and reconstructed peaks which is defined

$$\text{MLE} = \frac{1}{L} \sum_{l=1}^{\hat{L}} \min_d \left(d(\xi_l, \hat{\xi}_{\hat{l}}) \right)_{\hat{l}=1:\hat{L}}, \tag{VI.1}$$

where $d(\xi, \hat{\xi}_{\hat{l}}) = \|\xi - \hat{\xi}_{\hat{l}}\|_2$, $\hat{L}$ is the number of the reconstructed peaks $\hat{\xi}_{\hat{l}}$ and L the total number of the original peaks.

- The mean strength error (MSE) given by

$$\text{MSE} = \frac{1}{L}\sum_{l=1}^{L}\|\gamma_l - \hat{\gamma}_{\bar{l}}\| \text{ where } \bar{l} := \min_d \left(d(\xi_l, \hat{\xi}_{\hat{l}}) \right)_{\hat{l}=1:\hat{L}}. \qquad \text{(VI.2)}$$

For dense distributions of peaks, we employed the earth mover's distance (EMD) (Wasserstein metric) as a measure of dissimilarity between the original and the estimated peaks locations [68], [62].

D. Examples

Three different examples are presented to demonstrate the different stages of the proposed scheme. In the first example, we show step by step the estimation of the locations and amplitudes of five positive peaks (see Figure 12). In the second example, presented in Figure 13, we use the proposed apprach to recover both positive and negative peaks. In the last example in Figure 14, we illustrate the potential of the algorithm to deal with denser peak distributions.

In the example of Figure 12 and 13, the low resolution images were of size $[M \times M] = [40 \times 40]$. The first estimation solving the ℓ_1- norm minimization problem was performed in a uniform computational mesh (with $[N \times N] = [15 \times 15]$ number of nodes) as we can observe in the top row, middle image of Figure 12. In particular, in Figure 12 along the top row, starting from left to right, we can observe the initial low resolution image, next the numerical solution of the first iteration (denoted by $m = 0$) and then, the new computational domain after the first estimation marked with gray color. The nodes corresponding to the nonzero entries for vector c on the computational meshes were denoted with small blue circles and the original peaks were marked with $+$. The new computational area was defined using the elements where the blue circled nodes belonged to. The second row of Figure 12 illustrates the nonzero locations estimated by solving the minimization problem (A.4) and the corresponding updated computational supports for the first, second, third and forth iteration of the proposed approach. In the last row, we can observe the ℓ_1-norm estimation for the last iteration, the final high resolution image and the approximation of the peaks using the coordinates of the nonzero coefficients at the last iteration.

The reconstruction results (amplitudes and locations) are summarized in Table III. Based on them, we have that all the five peaks were recovered and their values are very close to the exact values.
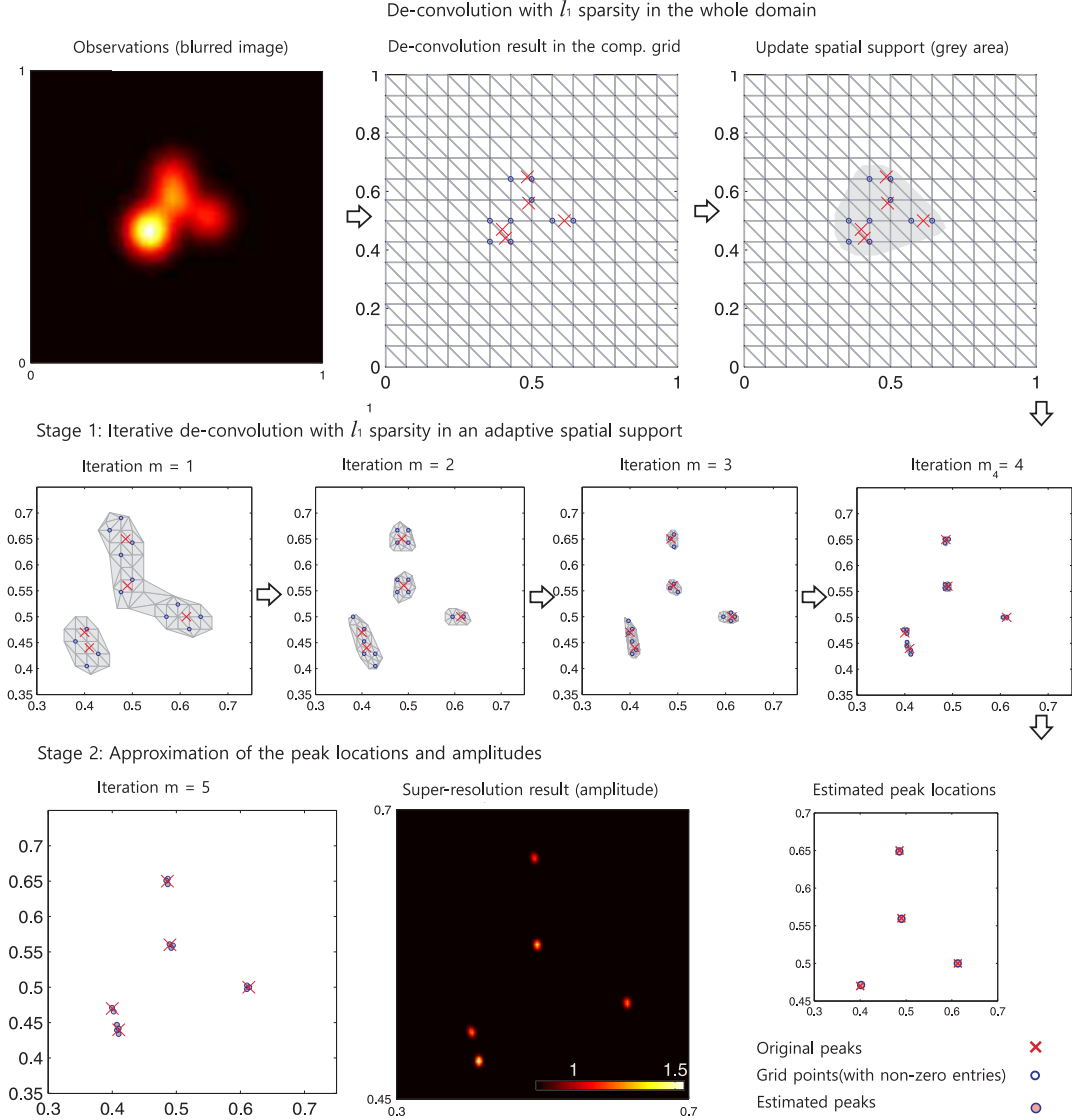
Fig. 12: Reconstruction of five positive peaks using the proposed adaptive super-resolution algorithm in a $[0,1]^2$ domain. Top row: the left image shows the observations on a $[40 \times 40]$ grid, the middle image shows the numerical solution of iteration $m = 0$ obtained solving the finite dimensional ℓ_1-norm minimization problem on a computational $[15 \times 15]$ domain. The right image depicts the new computational support in light grey color. Middle row: the left image shows the numerical solution of iteration $m = 1$ and the new computational support in light grey. Accordingly, the middle and right images show the numerical solution and the computational support of iteration $m = 2$ and $m = 3$ respectively. Bottom row: the left image shows the result of the last iteration, the middle image is the super-resolved results and the right image shows the exact and the estimated peaks image. Please note the limits of the axes have been updated in the images in order to focus in the area that the point sources are located.

Location		Amplitude	
ξ	$\hat{\xi}$	γ	$\hat{\gamma}$
(0.195,0.58)	(0.198,0.58)	1	0.99
(0.18,0.72)	(0.18,0.72)	1.5	1.51
(0.48,0.46)	(0.48,0.45)	1	1
(0.72,0.38)	(0.71,0.38)	1	0.98
(0.64,0.36)	(0.65,0.37)	1.2	1.2
MLE:	0.0049	MSE:	0.013

TABLE III: This table summarizes the results of the test case in Fig. 12. The first and the third columns show the locations and the amplitudes of the original peaks respectively and the second and forth column, the corresponding estimated values using the proposed approach. The last row shows the values of the MLE (equation VI.1) and MSE (equation VI.2)

To show that the proposed scheme can be used to recover both positive and negative peaks, Figure 13 illustrates the estimation of two positive and two negative peaks. The original peaks are marked with + for the positive peaks and x for the negative peaks and the estimated ones with circles and squares respectively in the right-hand side image of Figure 13. Table IV summarizes the values of the location and the amplitude of the original and the estimated peaks of the example in Figure 13. The estimated locations and amplitudes are very close to the original ones with small values for the metrics MLE and MSE for this setup. We further examined the proposed scheme
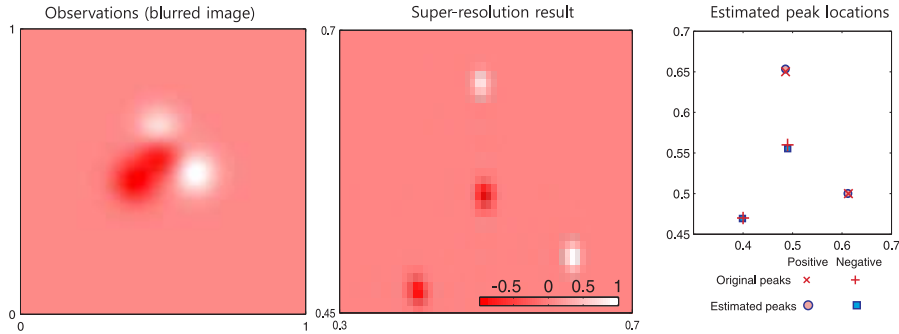

Fig. 13: Positive and negative peak reconstructions. Starting from left, the original low resolution image, estimated high resolution image and the locations of the actual and estimated peaks. Please note the limits of the axes have been updated in the middle and right image in order to focus in the area that the point sources are located

in the case where 50 peaks of intensity one were simulated. Figure 14 presents in a similar way as Figure 12 the progressive towards the recovery of the peaks. In this test, the low resolution image was $[M \times M] = [80 \times 80]$ and the first numerical estimation was performed in a uniform mesh

Location		Amplitude	
ξ	$\hat{\xi}$	γ	$\hat{\gamma}$
(0.49,0.56)	(0.4857,0.556)	-1	-0.9886
(0.486,0.65)	(0.4857,0.6533)	0.8	0.7528
(0.4,0.47)	(0.3989,0.4694)	-1	-0.9739
(0.613,0.5)	(0.612,0.5)	1	1.0076
MLE:	0.0025	MSE:	0.0231

TABLE IV: This table summarizes the results of the test case illustrated in Fig. 13. The first and the third columns show the locations and the amplitudes of the original peaks respectively and the second and forth column, their estimated values using the proposed approach. The last row shows the values of the MLE (equation VI.1) and MSE (equation VI.2)

with $[15 \times 15]$ nodes. Here, the middle row of Figure 12 shows the estimates in the first, second and ninth iteration. Also, the small lowermost right image illustrates how the numerical solution (blue circles) appears in a small area around 2 peaks. The total number of recovered peaks was 49. There is an omission due to the very close proximity of two peaks which appear as a single (more intense) peak in the lower right side of the image "super-resolution result". Very few of the peak intensities were more prominent than others. The EMD as a measure of dissimilarity between the actual and estimated point sources, in domain $[0,1]^2$, was $\text{EMD} = 0.01$ (or 1% dissimilarity between the true source distribution and the estimated one).

Finally by keeping the noise level at 40dB, we performed reconstructions using sets of low resolution images obtained from the convolution of randomly distributed sources with the same Gaussian kernel ($\alpha = 0.2$). The domain and the properties of the kernel were the same as in the test of Figure 14. Particularly, given the number of point sources, 50 randomly created source distributions were generated to produce 50 low resolution images. In Figure 15 we have the average EMD values in $\%$ estimated by comparing the true point sources with the estimated ones (left image) and the average number of reconstructed sources (right image) for increasing number of point sources.

Moreover, based on the histograms of Figure 16 we can observe when the number of point sources is low the localization error expressed through the EMD value is also low whereas when the number of point sources increases we have larger variation in the EMD and source number estimates. This can be explained by the very close proximity of some (true) point sources that can occur more likely when their number increases in the confined domain $[0,1]^2$. This can lead to difficulties in separating some of the point source from each other. Overall, our demonstrations
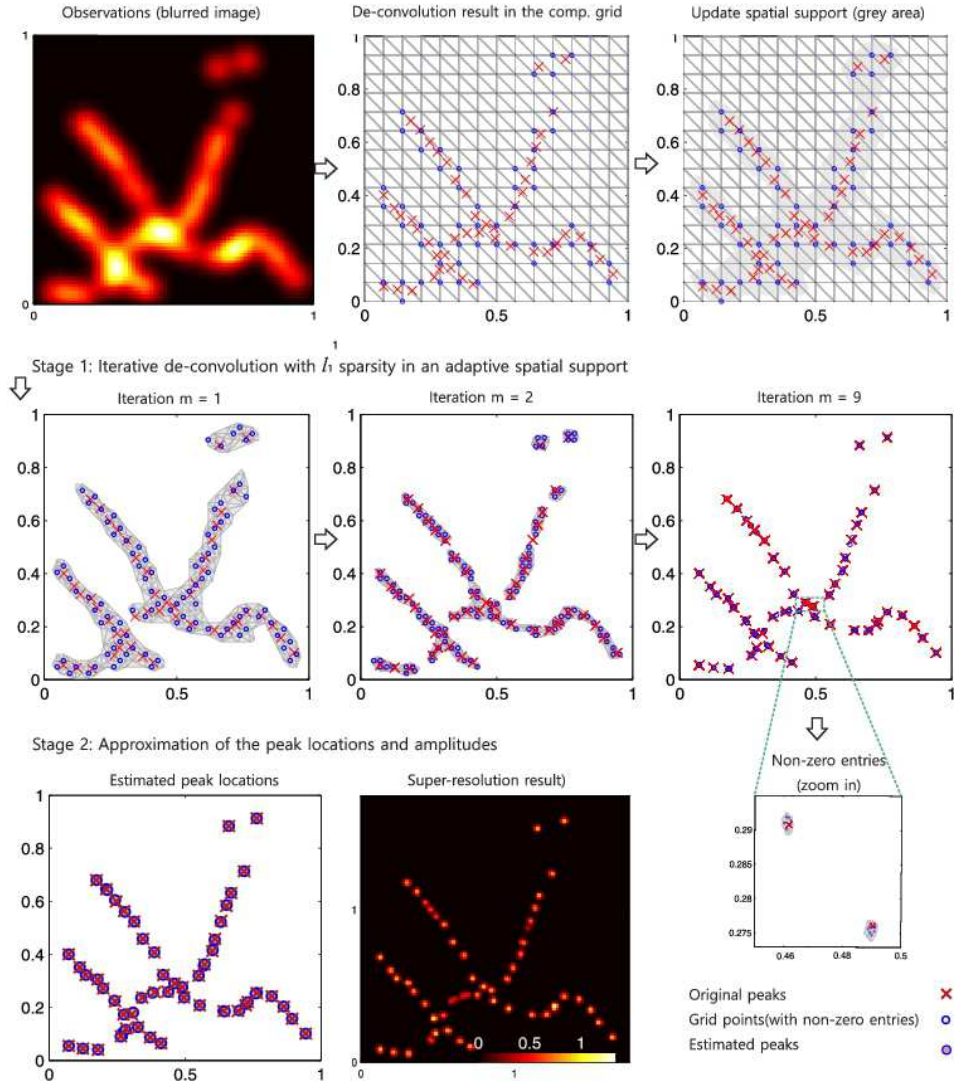
Fig. 14: Reconstruction of multiple peaks. The uppermost left images shows the original low resolution observations and similarly as it was described in Figure 12, we present the progressive steps of the approach to separate the underlying peaks. Also, the image on the lowermost left side shows the grid points corresponding to non-zero coefficients in the clusters (in grey) of the 9th iteration of the approach

indicate that, in a low noise regime, the proposed superresolution adaptive scheme can recover as many peaks as the exact number of them in most of the cases when their distance does not violate an underlying separation condition e.g. minimum distance $\Delta_{min} \geq C\sigma$ for Gaussian kernels [64]. Our numerical simulations showed that, when the noise level was SNR=40dB, the correct number of peaks could be recovered if $\Delta_{min}/\sigma > 0.2$ given h_M. We remark that even though the effect of
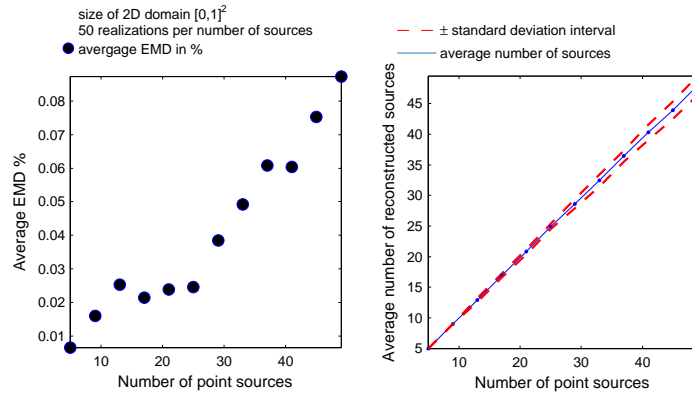
Fig. 15: Left image: Average EMD value in % and Right image: average number of sources for increasing number of simulated sources. 50 different realization per number of source were simulated.

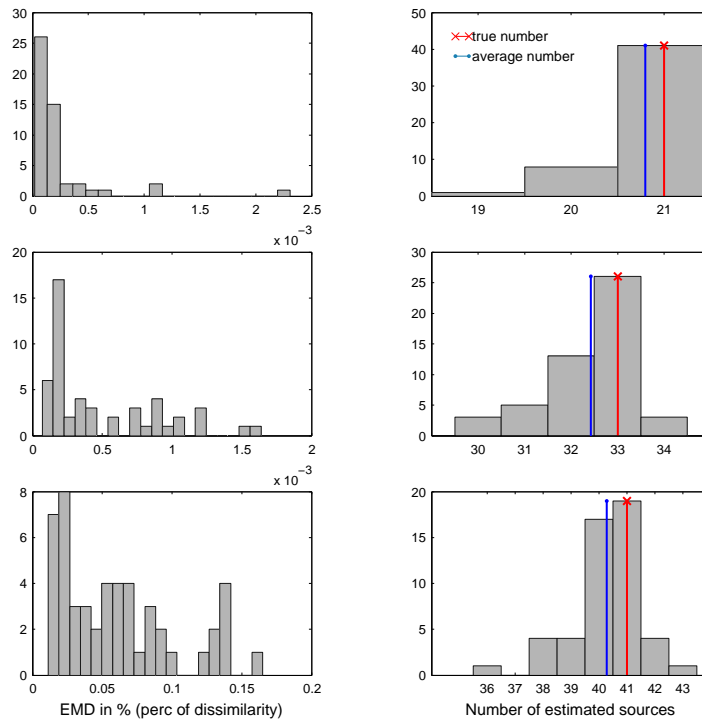Fig. 16: Histograms of estimated EMD values (left columns) and number of reconstructed sources (right column) when the number of simulated sources was 21, 33, 41 respectively starting from the top row.

the measurement noise (either Gaussian or Poisson) and the measurement/observation sampling can affect the recovery of a multi-dimensional signal, these mathematical questions admit of different

analysis than the currently addressed questions and will be considered in a follow-up study.

E. Discussion and future prospects

Questions regarding the deconvolution of sparse peaks present great mathematical difficulties with some of them investigated in studies such as in [26], [27], [28], [22], [65]. However, even though very important, these studies often do not accommodate easily accessible solutions to software developers and engineers working on superresolution applications. The current work aimed to shed light into some of these theoretical findings and put them into perspective with practical solutions in superresolution algorithms.

In the theoretical part of this study, we explained why clusters of nonzero peaks appear around the locations of the original peaks when we solve the ℓ_1-norm minimization problem on a discrete grid and in which parts of the grid these nonzero peaks are more likely to appear. Moreover, we showed how the locations of the underlying peaks are connected with the numerical solution using the optimality condition of the ℓ_1- norm minimization problem. One important remark here is that the distribution of the nonzero coefficients of the numerical solution depend on the properties of the convolution kernel $H = G * G$ (III.6) and not on kernel G (I.1). Therefore thinking in more general terms, for an inverse problem with forward operator R, it is only important that R^*R is a convolution to anticipate a numerical solution following similar pattern as in the current problem. This could be true for example in classical tomography e.g. filtered back-projection [59].

In general, we envision that similar superresolution schemes can be performed in a wide variety of inverse problems in the fields of geophysics, astronomy and spectroscopy [47], [35], [46] because many of these applications share the same characteristics and properties as this deconvolution problem. However, some new aspects need to be investigated. For example, in neuroimaging, the EEG source imaging problem, even though it shares seemingly similarities with the current deconvolution, problem, is a severely ill-posed problem where the forward operator has a singularity and its computational version has a matrix with a large null space [54]. Therefore, special design of the prior model (e.g. weighting) is required whereas the expected pattern of the numerical reconstructions has to be studied carefully.

In the application part, the main two novelties of the proposed approach were a) the automatic adaptation of the computational domain (using elements) and b) the approximation of the underlying peaks using a numerical approximation of the ℓ_1 norm optimality condition that stemmed from the findings of our theoretical analysis. As a natural next step though, within the microscopy field

we expect to compare the proposed approach with other state-of-the art algorithms [72] which lie either on the variational or spectral framework, e.g. Alternating Descent Conditional Gradient Method [10] or MUSICAL [1] respectively.

Moreover, we are considering extension that could improve the algorithmic performance, for example, the incorporation of a non-convex step as in [10] to possibly speed up the convergence. In that step possibly, the optimality curve (III.6) could guide the update of the computational domain simultaneously in multiple locations. Furthermore, the idea of employing the ensemble learning or committee method [58] (which allows to estimate a weighted solution in each discretization level by solving multiple deconvolution problems in a parallel fashion), could help to reduce possible bias introduced due to the regularization or high measurement noise.

VII. CONCLUSIONS

The current work bridges the gap between theoretical studies and implementations of algorithms that impose sparsity constraints on the signal to be recovered. First, we studied theoretically the deconvolution of single peaks using the ℓ_1- norm and we confirmed recent observations that a discrete reconstruction yields to multiple peaks at grid points adjacent to the location of the actual peak. We showed that by using these adjacent peaks and the first order optimality condition of this convex problem, we can obtain a set of linear equations to approximate the location of the actual peak. We quantified the errors between the continuous (TV) problem (that allows exact peak recoveries) and the finite ℓ_1- norm minimization problem, which designated that the accuracy of the numerical estimates depends on the discretization that can be improved by applying finer gridding.

Second, using the previous theoretical finding we proposed an iterative scheme in which automated local refinement on the computational grid was performed to identify the areas where the true peaks were located. Then, with the help of the equations from the optimality condition, the peak locations and amplitudes were estimated. Finally, low resolution images, obtained using simulated focal sources convoluted with a smooth kernel, were used to show that our approach can increase the spatial resolution by allowing the separation and localization of these focal sources.

APPENDIX

A. Proof of Theorem III.2

Proof.

Let us first consider that the reconstructed signal is $\mu^N = \alpha \delta_{x_K}$ with $a > 0$. When $j = K$, $p_K = 1$

in the optimality condition (II.8) since $p_K \in \partial c_K$ and $a = c_K > 0$. Thus, the optimality condition (II.8) reduces to

$$\lambda = \gamma H(x_K - \xi) - aH(0)$$
$$\Leftrightarrow \quad a = \frac{\gamma H(x_K - \xi) - \lambda}{H(0)} . \tag{A.1}$$

Now let us consider the case where $j = K + 1$, then (II.8) becomes

$$\lambda p_{K+1} = \gamma H(x_{K+1} - \xi) - aH(x_{K+1} - x_K) . \tag{A.2}$$

Since, we assumed only one non-zero coefficient of μ^N at x_K, we need to show that inequality condition $|p_{K+1}| < 1$ holds.

Inserting (A.1) into (A.2) yields

$$\lambda p_{K+1} = \gamma H(x_{K+1} - \xi) - \frac{\gamma H(x_K - \xi) - \lambda}{H(0)} H(h) ,$$

where $h = |x_K - x_{K+1}|$. For this equation we consider the second order Taylor expansion of H around zero. Note that $H'(0) = 0$ holds, due to the maximum of H at zero. Therefore, we obtain

$$\lambda p_{K+1} = \gamma H(0) + \frac{\gamma}{2} H''(0)(x_{K+1} - \xi)^2$$
$$- \left(\gamma + \frac{\gamma H''(0)}{2H(0)} (x_K - \xi)^2 \right) \left(H(0) + \frac{1}{2} H''(0)h^2 \right)$$
$$+ \lambda + \frac{\lambda}{2H(0)} H''(0)h^2 + \mathcal{O}(h^3) ,$$

which reduces to

$$p_{K+1} = 1 - \frac{\gamma}{2\lambda} H''(0)T + \mathcal{O}(h^3) ,$$

where $T = (x_K - \xi)^2 - (x_{K+1} - \xi)^2 + h^2 \left(1 - \frac{\lambda}{\gamma H(0)} \right)$. Note also that $H''(0) < 0$ as H attains its maximum at zero and $\lambda < \gamma H(0)$.

In order to obtain the inequality $|p_{K+1}| < 1$, which would prove the assertion, T has to be negative. This is true if and only if we have

$$x_K^2 - x_{K+1}^2 + 2\xi h < h^2 \left(\frac{\lambda}{\gamma H(0)} - 1 \right) .$$

This is equivalent to

$$2\xi h < h^2\left(\frac{\lambda}{\gamma H(0)} - 1\right) + (x_{K+1} + x_K)h$$

$$\Leftrightarrow \quad \xi < \frac{h}{2}\left(\frac{\lambda}{\gamma H(0)} - 1\right) + \frac{1}{2}x_{K+1} + \frac{1}{2}x_K$$

$$\Leftrightarrow \quad \xi - x_K < \frac{h}{2}\left(\frac{\lambda}{\gamma H(0)} - 1\right) + \frac{h}{2} .$$

Thus, we obtain

$$\xi - x_K < \frac{\lambda h}{2\gamma H(0)} < \frac{1}{2}h , \tag{A.3}$$

which is true since we have $\lambda < \gamma H(x_K - \xi)$ and $H(x_K - \xi) < H(0)$.

Now assume that h is sufficiently small in the latter case and make the Ansatz $\mu^N = c_K\delta_{x_K\mu^N=} + c_{K+1}\delta_{x_{K+1}}$. Without restriction of generality we consider $\gamma > 0$ hence we look for $c_K > 0$ and $c_{K+1} > 0$, the other sign is analogous. We extend the vector c by $c_j = 0$ for $j \notin \{K, K+1\}$ and verify that it is a minimizer of J in (I.5) by constructing an appropriate subgradient in the optimality condition (II.7).

In particular, we have

$$p_j = \frac{1}{\lambda}[A^*(f - Ac)]_j = p(x_j)$$

where

$$p(x) = \frac{\gamma}{\lambda}H(x - \xi) - \frac{c_K}{\lambda}H(x - x_K) - \frac{c_{K+1}}{\lambda}H(x - x_{K+1}) .$$

The conditions $p_K = p_{K+1} = 1$ lead to the following 2×2 system

$$\lambda = \gamma H(x_K - \xi) - c_K H(0) - c_{K+1}H(h)$$

$$\lambda = \gamma H(x_{K+1} - \xi) - c_K H(h) - c_{K+1}H(0) ,$$

for c_K and c_{K+1}. If h is sufficiently small, Taylor expansion of H around zero yields

$$H(0)(c_K + c_{K+1}) + \frac{h^2}{2}H''(0)c_{K+1} =$$
$$\lambda - \gamma H(0) - \gamma\frac{(x_K - \xi)^2}{2}H''(0) + \mathcal{O}(h^3)$$
$$H(0)(c_K + c_{K+1}) + \frac{h^2}{2}H''(0)c_K =$$
$$\lambda - \gamma H(0) - \gamma\frac{(x_{K+1} - \xi)^2}{2}H''(0) + \mathcal{O}(h^3) \ .$$

From the leading terms we obtain the solution

$$c_K = \frac{1}{2}\left(\gamma - \frac{\lambda}{H(0)} + \frac{x_K + x_{K+1} - 2\xi}{h}\right) + \mathcal{O}(h)$$
$$c_{K+1} = \frac{1}{2}\left(\gamma - \frac{\lambda}{H(0)} - \frac{x_K + x_{K+1} - 2\xi}{h}\right) + \mathcal{O}(h) \ .$$

Note also that $\gamma - c_K - c_{K+1} = \frac{\lambda}{H(0)} + \mathcal{O}(h)$.

This implies for $x \notin [x_K, x_{K+1}]$

$$p(x) = \frac{\gamma}{\lambda}H(x - \xi) - \frac{c_K}{\lambda}H(x - x_K) - \frac{c_{K+1}}{\lambda}H(x - x_{K+1})$$
$$= (\gamma - c_K - c_{K+1})\frac{H(x - \xi)}{\lambda} + \frac{c_K}{\lambda}H'(x - \xi)(x_K - \xi)$$
$$+ \frac{c_{K+1}}{\lambda}H'(x - \xi)(x_{K+1} - \xi) + \mathcal{O}(h^2) \ .$$

For $x - \xi$ small we can again apply Taylor expansion around zero to show that $0 \leq p(x) \leq 1$.

For $x - \xi$ large we find

$$p(x) = \frac{H(x - \xi)}{H(0)} + \mathcal{O}(h) \ ,$$

and since $0 \leq \frac{H(x-\xi)}{H(0)} < 1$ we find $p(x) \in (-1, 1)$ for grid size h sufficiently small. Thus, the optimality condition is satisfied on all grid points. $\qquad\square$

B. Adaptive superresolution approach: implementation

In the following description, index $m = 0, \ldots,$ denotes the mth-iteration of the adaptive superresolution approach. In m^{th} iteration, the computational domain is denoted by $\Omega^m \equiv (\mathcal{E}^m, \mathcal{N}^m)$ where $\mathcal{E}^m$ is the set that includes all the elements and $\mathcal{N}^m = \{x_k^m\}_{1:N^m}$ is the set with the corresponding nodes that describe domain Ω^m.

In m^{th} iteration

1) We solve the minimization problem

$$J_{\Omega^m}(c) = \frac{1}{2} \left(\sum_{j=1}^{M} \sum_{k=1}^{N^m} c_k G(x_j - x_k^m) - w_j \right)^2 + \lambda \|c\|_1, \qquad \text{(A.4)}$$

where the vector $c \in \mathbb{R}^{N^m}$ includes the nonzero coefficients of the recovered signal μ^N (I.3) at nodes x_k , $\|c\|_1 = \sum_{k=1}^{N^m} |c_k|$ and $w \in \mathbb{R}^M$, i.e. $w = \{f(z_j) + \varepsilon_j\}_{j=1,\ldots,M}$ is a sampled version of the observations f on a set of measurement nodes $\{z_j\}_{j=1,\ldots,M}$ and ε is the additive measurement noise.

2) Then, we update the computational domain.

First, we remove the redundant elements (i.e. elements where all their nodes correspond to zero entries in vector c). We define the new domain Ω^m by estimating a set of disjoint clusters $\Omega_{\hat{l}}^m \equiv (\mathcal{E}_{\hat{l}}^m, \mathcal{N}_{\hat{l}}^m)$ (groups of adjacent elements) which comprises the remaining elements. Hence, the update domain is $\Omega^m = \bigcup_{\hat{l}=1}^{\hat{L}_m} \Omega_{\hat{L}}^m$ where $\Omega_{\hat{l}}^m \bigcap_{\hat{l}=1}^{\hat{L}_m} = \emptyset$ and $\hat{L}^m$ is the total number of formed clusters.

The mesh refinement is performed by including extra points/nodes in each cluster $\Omega_{\hat{l}}^m$. The extra points/nodes are at the centroids of the elements that comprise the clusters. The centroids of very small elements are discarded. The choice of the centroids as extra nodes is based on the observation that if $c_k \neq 0$ at node x_k^m, then the original peak should be in the neighborhood of x_k^m (stemming from the analysis in section III-B). For each cluster $\Omega_{\hat{l}}^m$, a new set of elements is estimated using the updated set of nodes $\mathcal{N}_{\hat{l}}^m$ (old nodes and centroids). Then, we repeat step 1, i.e. we solve problem (A.4) in the updated sets of nodes $\mathcal{N}^m = \bigcup_{\hat{l}=1}^{\hat{L}_m} \mathcal{N}_{\hat{l}}^m$.

Steps 1-2 are repeated until the computational support is not longer updated (the number of nodes and elements stays fixed). This happens when the distance between the nodes becomes small. As a minimum distance (between two nodes) we can use a limit for peak separation presented for some convolution kernels in [64], [65]). Alternatively, prior information about the expected size of the underlying peaks (e.g. in microscopy the sizes of the molecules) can be considered. Then, we recover as many peaks as the number of the disjoint clusters $\Omega_{\hat{l}}$, for $\hat{l} = 1, \ldots, \hat{L}$ (where $\hat{L}$ is the total number of disjoint clusters estimated in the last iteration). The amplitude denoted by $\hat{\gamma}_{\hat{l}}$ in cluster $\Omega_{\hat{l}}$ follows from equation (IV.8) using the coefficients entries of that cluster. For the approximation of the the peak location in cluster $\Omega_{\hat{l}}$, we first check the number of nonzero

coefficients denoted by $N_{\hat{l}}$. If $N_{\hat{l}} > d$ (where d is the dimensionality of the problem), the peak location, $\hat{\xi}_l$, is estimated by solving a linear system formed using the expression (IV.9). Now, if $2 \leq N_{\hat{l}} \leq d$ then the peak location can be approximated with the help of linear basis functions, ϕ_k. If the approximated location is expressed as $\hat{\xi}_{\hat{l}} = \sum_{k=1}^{N_{\hat{l}}} \phi_k x_k$ then by inserting the previous linear representation for $\hat{\xi}_{\hat{l}}$ in expression (IV.9), we can obtain an approximation for the peak location. If $N_{\hat{l}} = 1$, then $\hat{\xi}_{\hat{l}}$ equals to the value of the nonzero node (following from (IV.3)).

ACKNOWLEDGEMENT

REFERENCES

[1] K. Agarwal and R. Macháň. Multiple signal classification algorithm for super-resolution fluorescence microscopy. *Nat. Commun.*, 7(1), Dec 2016.

[2] F. Andersson and M. Carlsson. ESPRIT for multidimensional general grids. *SIAM Journal on Matrix Analysis and Applications*, 39(3):1470–1488, Jan 2018.

[3] J.-M. Azais, Y. de Castro, and F. Gamboa. Spike detection from inaccurate samplings. *Appl. Comput. Harmon. Anal.*, 38(2):177–195, Mar 2015.

[4] O. Bar-Ilan and Y. C. Eldar. Sub-nyquist radar via doppler focusing. *IEEE Trans. Signal Process.*, 62(7):1796–1811, April 2014.

[5] T. Bendory. Robust recovery of positive stream of pulses. *IEEE Trans. Signal Process.*, 65(8):2114–2122, Apr 2017.

[6] T. Bendory, A. Bar-Zion, D. Adam, S. Dekel, and A. Feuer. Stable support recovery of stream of pulses with application to ultrasound imaging. *IEEE Trans. Signal Process.*, 64(14):3750–3759, Jul 2016.

[7] T. Bendory, S. Dekel, and A. Feuer. Super-resolution on the sphere using convex optimization. *IEEE Trans. Signal Process.*, 63(9):2253–2262, May 2015.

[8] T. Bendory, S. Dekel, and A. Feuer. Robust recovery of stream of pulses using convex optimization. *J. Math. Anal. Appl.*, 442(2):511–536, 2016.

[9] B. N. Bhaskar, G. Tang, and B. Recht. Atomic norm denoising with applications to line spectral estimation. *IEEE Trans. Signal Process.*, 61(23):5987–5999, Dec 2013.

[10] N. Boyd, G. Schiebinger, and B. Recht. The alternating descent conditional gradient method for sparse inverse problems. *SIAM Journal on Optimization*, 27(2):616–639, jan 2017.

[11] S. Boyd, N. Parikh, E. Chu, B. Peleato, and J. Eckstein. Distributed optimization and statistical learning via the alternating direction method of multipliers. *Machine Learning*, 3(1):1–122, 2010.

[12] S. Boyd and L. Vandenberghe. *Convex Optimization*. Cambridge University Press, 2004.

[13] K. Bredies and H. K. Pikkarainen. Inverse problems in spaces of measures. *ESAIM: Control, Optimization and Calculus of Variations*, 19:190–218, 2013.

[14] M. Burger, M. Moeller, and P. Heins. Locally sparse reconstruction using $\ell^{1,\infty}$-norms. *Inverse Problems and Imaging*, 9(4):1093–1137, Oct 2015.

[15] E. J. Candès and C. Fernandez-Granda. Super-resolution from noisy data. *Journal of Fourier Analysis and Applications*, 19(6):1229–1254, 2013.

[16] E. J. Candès and C. Fernandez-Granda. Towards a mathematical theory of super-resolution. *Commun. Pure Appl. Math.*, 67(6):906–956, Apr 2013.

[17] E. J. Candès, J. Romberg, and T. Tao. Robust uncertainty principles: exact signal reconstruction from highly incomplete frequency information. *IEEE Trans. Inf. Theory*, 52(2):489–509, Feb 2006.

[18] Y. De Castro, F. Gamboa, D. Henrion, and J. B. Lasserre. Exact solutions to super resolution on semi-algebraic domains in higher dimensions. *IEEE Trans. Inf. Theory*, 63(1):621–630, 2017.

[19] D. C. Champeney. *A handbook of Fourier theorems*. Cambridge University Press, 1989.

[20] Sc. Sh. Chen, D. L. Donoho, and M. A. Saunders. Atomic decomposition by basis pursuit. *SIAM Journal on Scientific Computing*, 20(1):33–61, 1998.

[21] Y. De Castro and F. Gamboa. Exact Reconstruction using Beurling Minimal Extrapolation. *Journal of Mathematical Analysis and Applications*, 395(1):Pages 336–354, November 2012.

[22] Q. Denoyelle, V. Duval, and G. Peyrè. Support recovery for sparse deconvolution of positive measures. *J. Fourier Anal. Appl.*, pages 1–42, 2016.

[23] B. Diederichs. Sparse frequency estimation: Stability and algorithms, phd thesis, 2018.

[24] D. L. Donoho. Superresolution via sparsity constraints. *SIAM J. Math. Anal.*, 23(5):13091331, 1992.

[25] V. Duval. A characterization of the non-degenerate source condition in super-resolution. *Information and Inference: A Journal of the IMA*, mar 2019.

[26] V. Duval and G. Peyré. Exact support recovery for sparse spikes deconvolution. Technical report, CNRS and Université Paris-Dauphine, July 2013.

[27] V. Duval and G. Peyré. Exact support recovery for sparse spikes deconvolution. *Foundations of Computational Mathematics*, 15(5):1315–1355, 2015.

[28] V. Duval and G. Peyré. The non degenerate source condition: Support robustness for discrete and continuous sparse deconvolution. In *IEEE International Workshop on Computational Advances in Multi-Sensor Adaptive Processing, Cancun, Mexico*, Dec. 2015.

[29] Vincent Duval and Gabriel Peyré. Sparse regularization on thin grids i: the lasso. *Inverse Problems*, 33(5):055008, Mar 2017.

[30] A. Eftekhari, T. Bendory, and G. Tang. Stable super-resolution of images: A theoretical study. *arxiv*, 2018.

[31] A. Eftekhari, J. Tanner, A. Thompson, B. Toader, and H. Tyagi. Sparse non-negative super-resolution — simplified and stabilised. *Applied and Computational Harmonic Analysis*, Aug 2019.

[32] C. Ekanadham, D. Tranchina, and E. P. Simoncelli. Recovery of sparse translation-invariant signals with continuous basis pursuit. *IEEE Trans. Signal Process.*, 59(10):4735–4744, Oct 2011.

[33] Ch. Ekanadham, D. Tranchina, and E. P. Simoncelli. A unified framework and method for automatic neural spike identification. *J. Neurosci. Methods*, 222:47–55, jan 2014.

[34] D. Elson, S. Webb, J. Siegel, K. Suhling, D. Davis, J. Lever, D. Phillips, A. Wallace, and P. French. Biomedical applications of fluorescence lifetime imaging. *Optics and Photonics News*, 12(11):26–32, 2002.

[35] H. W. Engl, M. Hanke, and A. Neubauer. *Regularization of Inverse Problems*. Kluwer Academic Publishers, 1996.

[36] C. Fernandez-Granda. Super-resolution of point sources via convex programming. *Jouranl of the IMP*, 2016.

[37] T. J. Gould, V. Verkhusha, and S. T. Hess. Imaging biological structures with fluorescence photoactivation localization microscopy. *Nat. Protocols*, 4(3):291–308, February 2009.

[38] Michael Grant and Stephen Boyd. CVX: Matlab software for disciplined convex programming, version 2.1. http://cvxr.com/cvx, March 2014.

[39] P. Heins. *Reconstruction using Local Sparsity: A Novel Regularization Technique and an Asymptotic Analysis of Spatial Sparsity Priors*. PhD thesis, PhD thesis, Westfälische Wilhelms Universität Münster (WWU Münster), 2014. 32.

[40] S. T. Hess, T. P.K. Girirajan, and M. D. Mason. Ultra-High Resolution Imaging by Fluorescence Photoactivation Localization Microscopy. *Biophysical Journal*, 91(11):4258–4272, 2006.

[41] H. Hindi. A tutorial on convex optimization II: duality and interior point methods. In *American Control Conference*, 2006.

[42] JB. Hiriart-Urruty, A. Korytowski, H. Maurer, and M. Szymkat, editors. *Advances in Mathematical Modeling, Optimization and Optimal Control*, volume 109, chapter Bregman Distances in Inverse Problems and Partial Differential Equations, pages 3–33. Springer, Cham, 2016.

[43] S. J. Holden, S. Uphoff, and A. N. Kapanidis. Daostorm: an algorithm for high- density super-resolution microscopy. *Nat Meth*, 8(4):279–280, April 2011.

[44] Y. Hua and T.K. Sarkar. Matrix pencil method for estimating parameters of exponentially damped/undamped sinusoids in noise. *IEEE Transactions on Acoustics, Speech, and Signal Processing*, 38(5):814–824, may 1990.

[45] S. A. Jones, S.-H. Shim, J. He, and X. Zhuang. Fast, three-dimensional super-resolution imaging of live cells. *Nat Meth*, 8(6):499–505, June 2011.

[46] J. P. Kaipio and E. Somersalo. *Statistical and Computational Inverse Problems*. Applied Mathematical Series. Springer, 2004.

[47] A. Kirsch. *An introduction to the mathematical theory of inverse problems*. Springer-Verlag New York., NY, USA, 1996.

[48] K. Koh, S.-J. Kim, and S. Boyd. An Interior-Point Method for Large-Scale L1-Regularized Logistic Regression. *Journal of Machine Learning Research*, 2007.

[49] H. Krim and M. Viberg. Two decades of array signal processing research: the parametric approach. *IEEE Signal Processing Magazine*, 13(4):67–94, jul 1996.

[50] Stefan Kunis, Thomas Peter, Tim Rmer, and Ulrich von der Ohe. A multivariate generalization of prony's method. *Linear Algebra and its Applications*, 490:31–47, feb 2016.

[51] W. Li, W. Liao, and A. Fannjiang. Super-resolution limit of the ESPRIT algorithm. *IEEE Transactions on Information Theory*, 66(7):4593–4608, jul 2020.

[52] Z. Li, Q. Peng, B. Bhanu, Q. Zhang, and H. He. Super resolution for astronomical observations. *Astrophysics and Space Science*, 363(5), Apr 2018.

[53] Wenjing Liao. Music for multidimensional spectral estimation: stability and super-resolution. *arxiv*, 2015.

[54] C. M. Michel, M. M. Murray, G. Lantz, S. Gonzalez, L. Spinelli, and R. Grave De Peralta. EEG source imaging. *Clin Neurophysiol*, 115(10):2195–2222, 2004.

[55] J. Min, C. Vonesch, H. Kirshner, L. Carlini, N. Olivier ans S. Holden, S. Manley, J.Chul Ye, and M. Unser. FALCON: fast and unbiased reconstruction of high-density super-resolution microscopy data. *Nature, Scientic Reports*, 4, 2014.

[56] V. I. Morgenshtern and E. J. Candès. Super-resolution of positive sources: The discrete setup. *SIAM J. Imag. Sci.*, 9(1):412–444, 2016.

[57] E. A. Mukamel, H. Babcock, and X. Zhuang. Statistical deconvolution for superresolution fluorescence microscopy. *Biophysics Journal*, 102:23912400, 2012.

[58] K. P. Murphy. *Machine Learning*. MIT Press Ltd, 2012.

[59] F. Natterer. *The mathematics of computerized tomography*. Society for Industrial and Applied Mathematics, Philadelphia, PA, USA, 2001.

[60] S. Osher, M. Burger, D. Goldfarb, J. Xu, and W. Yin. An iterative regularization method for total variation-based image restoration. *Multiscale Modeling '& Simulation*, 4(2), 2005.

[61] M. Ovesny, P. Krizek, J. Borkovec, Z. Svindrych, and G.M. Hagen. Thunderstorm: a comprehensive imagej plugin for palm and storm data analysis and super-resolution imaging. *Bioinformatics*, 30:2389–2390, 2014.

[62] O. Pele and M. Werman. Fast and robust earth mover's distances. In *Proceeding of the IEEE International Conference on Computer Vision*, pages 460–467, 2009.

[63] Thomas Peter, Gerlind Plonka, and Robert Schaback. Prony's method for multivariate signals. *PAMM*, 15(1):665–666, Oct 2015.

[64] Cl. Poon, N. Keriven, and G. Peyré. A dual certificates analysis of compressive off-the-grid recovery. *Arxiv*.

[65] Cl. Poon and G. Peyré. MultiDimensional sparse super-resolution. *SIAM Journal on Mathematical Analysis*, 51(1):1–44, jan 2019.

[66] R. Roy and T. Kailath. Esprit-estimation of signal parameters via rotational invariance techniques. *IEEE Transactions on Acoustics, Speech, and Signal Processing*, 37(7):984–995, Jul 1989.

[67] R.Tibshirani. Regression shrinkage and selection via the lasso. *Journal of the Royal Statistical Society: Series B (Methodological)*, 58(1):267–288, jan 1996.

[68] Yossi Rubner, Carlo Tomasi, and Leonidas J. Guibas. The Earth Mover's Distance as a Metric for Image Retrieval. *International Journal of Computer Vision*, 40(2):99–121, 2000.

[69] M. J. Rust, M. Bates, and X. Zhuang. Sub-diffraction-limit imaging by stochastic optical reconstruction microscopy (STORM). *Nature Methods*, 3:793–796, 2006.

[70] D. Sage, H. Kirshner, T. Pengo, N. Stuurman, J. Min, S. Manley, and M. Unser. Quantitative evaluation of software packages for single-molecule localization microscopy. *Nat Meth*, 12(8):717–724, 8 2015.

[71] R. Schmidt. Multiple emitter location and signal parameter estimation. *IEEE Transactions on Antennas and Propagation*, 34(3):276–280, mar 1986.

[72] A. Small and S. Stahlheber. Fluorophore localization algorithms for super-resolution microscopy. *Nat. Methods*, 11:267–279, 2014.

[73] P. Stoica and R. Moses. Spectral analysis of signals. *Prentice Hall*, 2005.

[74] G. Tang, B. N. Bhaskar, and B. Recht. Sparse recovery over continuous dictionaries-just discretize. In *2013 Asilomar Conference on Signals, Systems and Computers*. IEEE, Nov 2013.

[75] G. Tang, B. N. Bhaskar, P. Shah, and B. Recht. Compressed sensing off the grid. *IEEE Trans. Inf. Theory*, 59(11):7465–7490, Nov 2013.

[76] J.-D. Tournier, F. Calamante, D. G. Gadian, and A. Connelly. Direct estimation of the fiber orientation density function from diffusion-weighted mri data using spherical deconvolution. *Neuroimage*, 23(3):1176 – 1185, 2004.

[77] U. Trottenberg, C. W. Oosterlee, and A. Schuller. Multigrid. Academic Press, 1st edition, 2000.

[78] R. Tur, Y. C. Eldar, and Z. Friedman. Innovation rate sampling of pulse streams with application to ultrasound imaging. *IEEE Transactions on Signal Processing*, 59(4):1827–1842, April 2011.

[79] N. Wagner, Y. C. Eldar, A. Feuer, and Z. Friedman. Compressed beamforming with applications to ultrasound imaging. In *2012 IEEE International Conference on Acoustics, Speech and Signal Processing (ICASSP)*, pages 3641–3644, March 2012.

[80] Wotao Yin, Stanley Osher, Donald Goldfarb, and Jerome Darbon. Bregman iterative algorithms for l1-minimization with applications to compressed sensing. *SIAM J. Imaging Sci*, pages 143–168, 2008.

[81] L. Zhu, W. Zhang, D. Elnatan, and B. Huang. Faster STORM using compressed sensing. *Nat. Methods*, 9(7):721–3, Apr 2012.